

Heat Transfer in a Rotary Drum Using Infrared Camera Temperature Measurement

by

Brandon Richard Boepple

A Thesis Presented in Partial Fulfillment  
of the Requirements for the Degree  
Master of Science

Approved April 2019 by the  
Graduate Supervisory Committee:

Heather Emady, Chair  
Christopher Muhich  
Julianne Holloway

ARIZONA STATE UNIVERSITY

May 2019

## ABSTRACT

Rotary drums are commonly used for their high heat and mass transfer rates in the manufacture of cement, pharmaceuticals, food, and other particulate products. These processes are difficult to model because the particulate behavior is governed by the process conditions such as particle size, particle size distribution, shape, composition, and operating parameters, such as fill level and rotation rate. More research on heat transfer in rotary drums will increase operating efficiency, leading to significant energy savings on a global scale.

This research utilizes infrared imaging to investigate the effects of fill level and rotation rate on the particle bed hydrodynamics and the average wall-particle heat transfer coefficient. 3 mm silica beads and a stainless steel rotary drum with a diameter of 6 in and a length of 3 in were used at fill levels of 10 %, 17.5 %, and 25 %, and rotation rates of 2 rpm, 6 rpm, and 10 rpm. Two full factorial designs of experiments were completed to understand the effects of these factors in the presence of conduction only (Case 1) and conduction with forced convection (Case 2). Particle-particle friction caused the particle bed to stagnate at elevated temperatures in Case 1, while the inlet air velocity in Case 2 dominated the particle friction effects to maintain the flow profile. The maximum heat transfer coefficient was achieved at a high rotation rate and low fill level in Case 1, and at a high rotation rate and high fill level in Case 2. Heat losses from the system were dominated by natural convection between the hot air in the drum and the external surroundings.

## DEDICATION

I dedicate this thesis to my family, for their endless love and support of my education.

## ACKNOWLEDGMENTS

I would like to thank my incredible professor and mentor, Dr. Emady, for her advice and support over the last four years. Manogna Adepu, for her guidance through technical concepts and revisions, and for developing the MATLAB code used in this research. Bradley Fox, for his help with experiments, analysis, and developing the MATLAB code. Andrew Swedler, for his help with experiments and analysis. Last but not least, Fred Peña, a teacher and friend, who has always been around to lend a helping hand. Thank you all.



## TABLE OF CONTENTS

	Page
LIST OF TABLES .....	vi
LIST OF FIGURES .....	vii
LIST OF SYMBOLS .....	ix
CHAPTER	
1 INTRODUCTION .....	1
Particulates .....	1
Mixing in Rotary Drums.....	2
Heat Transfer in Rotary Drums .....	4
Temperature Measurement .....	5
Background .....	6
2 MATERIALS .....	10
Rotary Drum .....	10
Auxiliary Materials .....	12
3 METHODS .....	15
Calibration Procedures.....	15
Experimental Procedures .....	18
Design of Experiments.....	19
Analytical Procedures .....	21

CHAPTER	Page
4 RESULTS AND DISCUSSION .....	22
Flow Profile.....	22
Wall-Particle Heat Transfer Coefficient.....	23
Fluid-Particle Heat Transfer Coefficient.....	29
5 CONCLUSION AND FUTURE WORK .....	31
Conclusion .....	31
Future Work.....	32
REFERENCES .....	33
APPENDIX	
A CALCULATIONS .....	35
B RAW DATA .....	44

## LIST OF TABLES

Table		Page
1.	Conditions for Flow Regimes in a Rotary Drum .....	4
2.	Heat Gun Settings .....	13
3.	Full Factorial DOE with Randomized Run Order for Case 1 and Case 2 .....	20
4.	Observed and Theoretical Flow Profiles Based on Fr And Table 1 .....	22

## LIST OF FIGURES

Figure	Page
1.	Cross-Section of a Typical Industrial Rotary Drum .....2
2.	Rotary Drum Design ..... 11
3.	Quartz Window Specifications with Air Inlet Hole in the Center ..... 12
4.	Rotary Drum Experimental Setup..... 14
5.	Particle Calibration Setup ..... 16
6.	Wall Calibration Setup..... 17
7.	Schematic of the Two Experimental Setups Used..... 18
8.	Region of Interest Selection for the Drum Wall and Particle Bed.....21
9.	Average Wall-Particle Heat Transfer Coefficient for Each Combination of Fill Level and Rotation Rate.....25
10.	Contour Plot of the Average Wall-Particle Heat Transfer Coefficient as a Function of Fill Level and Rotation Rate for Case 2, Using the Window with Holes .....27
11.	Contour Plot of the Average Wall-Particle Heat Transfer Coefficient as a Function of Fill Level and Rotation Rate for Case 1, Using the Window with Holes .....28
12.	Contour Plot of the Average Wall-Particle Heat Transfer Coefficient as a Function of Fill Level and Rotation Rate for Case 1, Using the Window without Holes .....29
A1.	Mass of 3 mm Silica Beads Required for Fill Levels from 10 – 25 % .....36
A2.	Particle Temperature Calibration Curves.....37

Figure	Page
A3. Wall Temperature Calibration Curves .....	37
A4. Infrared Counts as a Function of Distance from Object at 50 °C and 100 °C ..	38
A5. Image of a 25 % Fill Level, 10 rpm Run Used to Determine $e_s$ .....	38
B1-B26. Raw Data for Case 1 Experiments.....	45-57
B27-B53. Raw Data for Case 2 Experiments.....	58-71

## LIST OF SYMBOLS

Symbol		Page
1.	Drum Rotation Rate, $\omega$ .....	2
2.	Drum Radius, $R$ .....	2
3.	Froude Number, $Fr$ .....	3
4.	Gravitational Force, $g$ .....	3
5.	Particle Bed Mass, $m_s$ .....	4
6.	Particle Specific Heat Capacity, $C_{ps}$ .....	4
7.	Average Particle Bed Temperature, $T_s$ .....	4
8.	Wall-Particle Conductive Heat Transfer Rate, $\dot{Q}_{wp}$ .....	4
9.	Particle-Particle Conductive Heat Transfer Rate, $\dot{Q}_{pp}$ .....	4
10.	Particle-Fluid-Particle Conductive Heat Transfer Rate, $\dot{Q}_{pfp}$ .....	4
11.	Fluid-Particle Convective Heat Transfer Rate, $\dot{Q}_{fpv}$ .....	4
12.	Average Wall-Particle Heat Transfer Coefficient, $\alpha_s$ .....	5
13.	Fraction of the Drum Wall Touched by Particles, $e_s$ .....	5
14.	Drum Circumference, $A_s$ .....	5
15.	Drum Length, $L$ .....	5
16.	Inner Drum Wall Temperature, $T_w$ .....	5
17.	Nusselt Number, $Nu$ .....	8
18.	Fluid-Particle Heat Transfer Coefficient, $h_f$ .....	8
19.	Fluid Thermal Conductivity, $k_f$ .....	8
20.	Fluid Reynolds Number, $Re_f$ .....	8

Symbol	Page
21. Particle Diameter, $d_p$ .....	8
22. Fluid Velocity, $u_f$ .....	8
23. Fluid Density, $\rho_f$ .....	8
24. Fluid Viscosity, $\mu_f$ .....	8
25. Biot Number, $Bi$ .....	8
26. Particle Radius, $r_p$ .....	8
27. Particle Thermal Conductivity, $k_p$ .....	8
28. Solids Fraction, $\phi$ .....	36
29. Particle Density, $\rho_p$ .....	36
30. Fill Level Fraction, $F$ .....	36
31. Chord Length, $C$ .....	39

# CHAPTER 1

## INTRODUCTION

### **Particulates**

Particulates are solid materials that exhibit properties of solids, liquids, and gases due to their ability to deform like a solid, flow like a liquid, and compress like a gas. They vary significantly in size, from fine powders to large rocks and boulders. The characteristics of each particulate system are different and depend on the material composition, particle size, particle size distribution, and shape, to name a few factors. For example, a single grain of sand may behave much differently than a sandbox. Applying enough downward force to a single sand particle will likely shear it into multiple smaller particles. The same force applied to a sandbox will do nothing but force the particles to compress without breakage. This pseudo-random nature of particulates is what makes them challenging to study and model compared to conventional solids, liquids, and gases (Rhodes, 2008).

Many industries use particulates to create an array of products. Powders are present in the pharmaceutical, cement, food, and cosmetic industries, among many others. Each industry may utilize different unit processes involving heat and mass transfer between particles. The rotary drum is one example of a common piece of equipment used for heating, drying, agglomeration, and reacting (Rhodes, 2008). One specific application is the production of cement clinker. According to the International Energy Agency (2019), this process requires more than 3 GJ per ton of clinker produced. In 2016, the cement industry consumed about  $10^{19}$  J, or 2 % of global energy consumption.



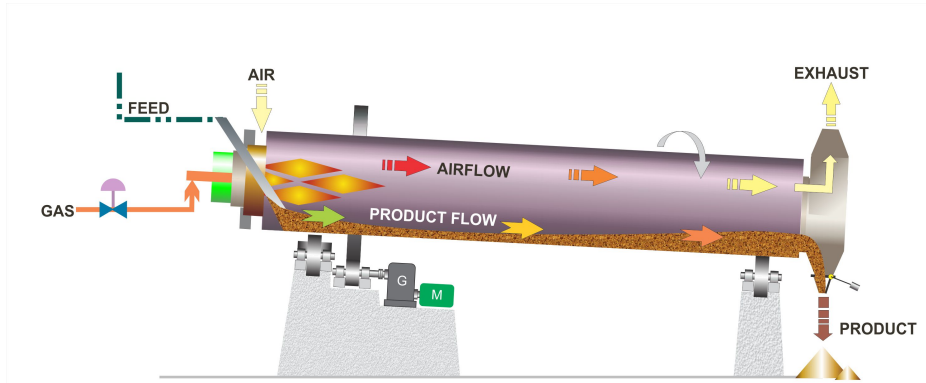


Figure 1. Cross-section of a typical industrial rotary drum (The Process for Making Portland Cement, 2018).

A typical industrial setup for a rotary drum is displayed in Figure 1. Rotary drums are usually inclined to allow the solid product to flow in one side and out the other. The heat source may be direct, where a hot gas stream is fired directly into the interior of the drum; indirect, where the exterior drum wall is heated and subsequently heats the material inside the drum; or some combination of both.

Large energy requirements and insufficient models necessitate a high demand for research on rotary drums. Even minuscule increases in operating efficiency can result in dramatic energy savings due to the large global scale of particulate processing. A challenge is that companies do not want to shut down processes for optimization research because shut down results in lost revenue. Therefore, more research is needed at the lab and pilot plant scale to improve these processes.

### **Mixing in Rotary Drums**

An essential characteristic of rotary drums is their ability to effectively mix the drum contents. Mixing occurs in different forms, dependent on the flow of the particles inside the drum. The drum rotation rate,  $\omega$ , drum radius,  $R$ , particle size, and fill level all

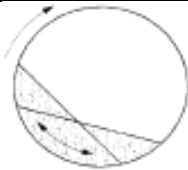
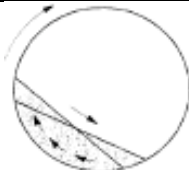
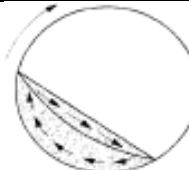

influence the hydrodynamics of particles. The Froude number,  $Fr$ , is a dimensionless ratio of the centrifugal force to gravity,  $g$ , and describes the flow regimes inside the drum for various rotation rates (Mellman, 2001).

$$Fr = \frac{\omega^2 R}{g} \quad (1)$$

The flow regimes relevant to this study are surging, slumping, rolling, and cascading. Table 1 below describes the conditions for these flow regimes (Mellman, 2001). At low rotation rates and fill levels, the particle bed does not mix, but slides along the drum wall as one body. With some wall roughness, friction causes the bed to oscillate at some frequency along the drum wall, still without any mixing. This is the surging regime. The bed movement transitions from surging to slumping as the rotation rate increases and the particles at the top of the particle bed have enough momentum to cause small avalanches down the top surface of the bed. At higher rotation rates, rolling motion is characterized by a uniform flow of particles along the drum wall to the top of the bed, which then roll down the top face and mix into the bed or contact the wall and repeat this process. For even higher rotation rates, the bed may exhibit a cascading motion. Cascading occurs when the top of the bed begins to arch. Most rotary kilns and reactors operate in the slumping, rolling, or cascading regimes to maximize particle contacts, increasing transport and reaction kinetics. There is no practical use for the surging regime, so it should be avoided by increasing the rotation rate. Rolling motion is preferred to achieve a well-mixed particle bed.

Table 1

*Conditions for flow regimes in a rotary drum (Mellman, 2001).*

	Surging	Slumping	Rolling	Cascading
				
<i>Fr</i>	$< 10^{-4}$	$10^{-5} - 10^{-3}$	$10^{-4} - 10^{-2}$	$10^{-3} - 10^{-1}$
Fill level	$> 10\%$	$< 10\%$	$> 10\%$	$> 10\%$

### Heat Transfer in Rotary Drums

Heat transfer may occur via three mechanisms: conduction, convection, and radiation. Radiation is only significant at temperatures above roughly 600 °C, which is outside the operating range of this study. Therefore, the heat transfer mechanisms studied in this work that are present in moderate temperature rotary drum applications are wall-particle conduction, particle-particle conduction, particle-fluid-particle conduction, and fluid-particle convection. Equation 2 describes the heat transfer mechanisms in the rotary drum system (Musser, 2011).

$$m_s C_{ps} \frac{dT_s}{dt} = \dot{Q}_{wp} + \dot{Q}_{pp} + \dot{Q}_{pfp} + \dot{Q}_{fpv} \quad (2)$$

In the above heat balance,  $m_s$  is the particle bed mass,  $C_{ps}$  is the particle specific heat capacity,  $T_s$  is the average particle bed temperature,  $\dot{Q}_{wp}$  is the wall-particle conductive heat transfer rate,  $\dot{Q}_{pp}$  is the particle-particle conductive heat transfer rate,  $\dot{Q}_{pfp}$  is the particle-fluid-particle conductive heat transfer rate, and  $\dot{Q}_{fpv}$  is the fluid-particle convective heat transfer rate. When the interstitial fluid is stagnant and its thermal conductivity is small compared to the particle bed,  $\dot{Q}_{pfp}$  and  $\dot{Q}_{fpv}$  are negligible

(Chaudhuri, Muzzio, & Tomassone, 2010). This yields the following heat balance equation,

$$m_s C_{ps} \frac{dT_s}{dt} = \alpha_s e_s A_s L (T_w - T_s) \quad (3)$$

where  $\alpha_s$ ,  $e_s$ ,  $A_s$ ,  $L$ , and  $T_w$ , are the average wall-particle heat transfer coefficient, fraction of the drum wall touched by particles, drum circumference, drum length, and inner drum wall temperature, respectively. The wall-particle heat transfer coefficient can be calculated from the slope by plotting the natural log of the normalized particle bed temperature against time.

$$\ln \left( \frac{T_w - T_s}{T_w - T_s^0} \right) = - \frac{\alpha_s e_s A_s L}{m_s C_{ps}} t \quad (4)$$

### **Temperature Measurement**

Previous work with this rotary drum setup used thermocouples to measure the temperature of the particle bed (Chaudhuri et al., 2010). This method proved to be inaccurate due to process downtime for measurement since the rolling had to stop to insert thermocouples into the particle bed. Notable heat loss occurred in the system, and the mixing profile was interrupted. An improvement implemented in this study is the use of an infrared camera to gather temperature data.

An infrared camera is a noninvasive temperature measurement device that measures infrared energy and reports it as a temperature value. A calculation must be done in order to report a temperature value from an energy measurement. To understand the calculation, it is necessary to discuss how objects emit infrared energy. A heated body such as a hot particle in the rotary drum emits infrared energy in all directions. When this energy contacts other objects, such as other particles, the drum wall, or the drum window,

the energy is absorbed, reflected, or transmitted through the object. For this emitted energy to reach the sensor in the infrared camera, it must pass through the drum window and the atmosphere between the window and the camera lens. Therefore, the calculated temperature value is a function of the emissivity of the particles, the transmission of the window, and the conditions of the atmosphere between the window and the camera. Since the emissivity is a function of temperature, a rigorous calibration must be performed in order to obtain true temperature values over a range of temperatures.

## **Background**

Many researchers have investigated the heating of solid materials in rotary drums. Wes, Drinkenburg, and Stermerding (1976) were some of the first to experimentally study heat transfer in a rotary drum. They assumed radial conduction dominates so there are negligible axial deviations in temperature, which is a widely accepted assumption today. They also developed the mathematical treatment for calculating the average wall-particle heat transfer coefficient, shown in Equation 4.

Most of the available data is based on simulations with short run time since particulate systems are complex and computationally intensive. Emady et al. (2016) found that increasing the rotation rate up to 10 rpm increased the heat transfer coefficient in their simulations. They concluded that materials with larger thermal conductivities exhibited more significant responses to changes in the rotation rate. Nguyen, Cosson, Lacrampe, and Krawczak (2015) concluded the particle heating rate increased with larger rotation rates, lower fill levels, and smaller particle sizes. Chaudhuri et al. (2010) employed simulations and experiments to show that rotation rate minimally increased the particle heating rate in a rotary drum with lifters attached to the inside wall. Njeng, Vitu,

Clausse, Dirion, and Debacq (2018) found that the heat transfer coefficient increased as the rotation rate increased to 10 rpm from experiments in their rotary drum with lifters. These researchers have shown via simulations and experiments in various conditions that the overall wall-particle heat transfer coefficient is on the order of 10-100 W/(m<sup>2</sup>K) and increases with increasing rotation rate and decreasing fill level.

The above findings are based on the assumption that radial conduction from the drum wall to the particle bed is the dominant heat transfer mechanism. This is assumed to be valid when there is no forced flow into the drum, so the interstitial and head space fluid are considered stagnant (Musser, 2011). There have been efforts to quantify the heat transfer coefficient due to convection between the particle bed and fluid (air) and between the wall and fluid. The fluid-particle convective heat transfer coefficient was calculated to be about 3 W/(m<sup>2</sup>K) by Debacq, Thammavong, Vitu, & Dupoizat (2011). Shi, Vargas, & McCarthy (2008) over-estimated the fluid-particle convective heat transfer coefficient to be a maximum of 8 W/(m<sup>2</sup>K). Calculations for the wall-fluid heat transfer coefficient were less than 1 W/(m<sup>2</sup>K) (Njeng et al., 2018). Since these heat transfer coefficients are at least 1 order of magnitude smaller than typical values for the wall-particle conductive heat transfer coefficient, the effects of fluid-particle and wall-particle convection are neglected when there is no moving fluid in the drum.

Shi et al. (2008) calculated the fluid-particle heat transfer coefficient using correlations for the Nusselt number. For low fluid velocities ( $Re_f < 100$ ),

$$Nu = \frac{h_f d_p}{k_f} = 0.03 Re_f^{1.3} \quad (5)$$

where  $Nu$ ,  $h_f$ ,  $k_f$ , and  $Re_f$  are the Nusselt number, fluid-particle heat transfer coefficient, fluid thermal conductivity, and fluid Reynolds number, respectively. The Reynolds number is calculated by

$$Re_f = \frac{d_p u_f \rho_f}{\mu_f} \quad (6)$$

where  $d_p$ ,  $u_f$ ,  $\rho_f$ , and  $\mu_f$  are the particle diameter, fluid velocity, fluid density, and fluid viscosity, respectively. The fluid velocity may be calculated using the following estimation.

$$u_f = \omega R \quad (7)$$

In this case, the velocity at the wall-fluid interface represents an over-estimation for the bulk fluid velocity.

The Biot number is calculated to show that the internal resistance is low for silica, indicating that the particles heat as isothermal bodies with no internal temperature gradient (Shi et al., 2008; Chaudhuri et al., 2010; Oschmann & Kruggel-Emden, 2018). The Biot number can be calculated using,

$$Bi = \frac{h_f r_p}{k_p} \quad (8)$$

where  $Bi$ ,  $r_p$ , and  $k_p$  are the Biot number, particle radius, and particle thermal conductivity, respectively. As the particle thermal conductivity increases and the particle size decreases,  $Bi$  approaches 0. For  $Bi \ll 1$ , the isothermal particle assumption is valid.

The available experimental data in this field relies exclusively on thermocouples to measure temperatures of particulate systems. Some researchers have used imaging techniques to study the flow behavior of particulate systems, such as Lueptow, Akonur,

and Shinbrot (2000). However, there is a lack of research employing infrared thermal imaging techniques to rotary drum applications. This research aims to fill the gap by providing a new method for studying the heat transfer mechanisms in the rotary drum using an infrared camera. The wall-particle heat transfer coefficient is calculated using Equation 4 to understand the effects of conduction, convection, fill level, and rotation rate on heat transfer in the rotary drum.



## CHAPTER 2

### MATERIALS

#### **Rotary Drum**

The rotary drum used in this study was inspired by Chaudhuri et al. (2010), who investigated conductive heating in rotary drums via simulations and experimental validation. This design was modified to allow insertion of hot air via a hole in one of the windows. The drum has a stainless steel core with an inner diameter of 6 in., a length of 3 in., and a thickness of 0.5 in. The core is supported by two 11 in. titanium wheels, which allow the drum to rotate without the core contacting the rollers. Stainless steel is mainly used for industrial rotary drums for its high thermal conductivity and corrosion resistance (Rotary Dryers, 2018). Titanium wheels, window plates, and bolts are used because titanium is lighter, less conductive, and more durable than stainless steel. The titanium components are meant to protect and insulate the stainless steel drum. There are two 6 mm thick windows on either end of the drum that are able to withstand up to 1200 °C; one is quartz and the other is sapphire. The quartz window is 6.5 in. in diameter and the sapphire window is 6 in. in diameter. Figure 2 shows various views of the drum apparatus.

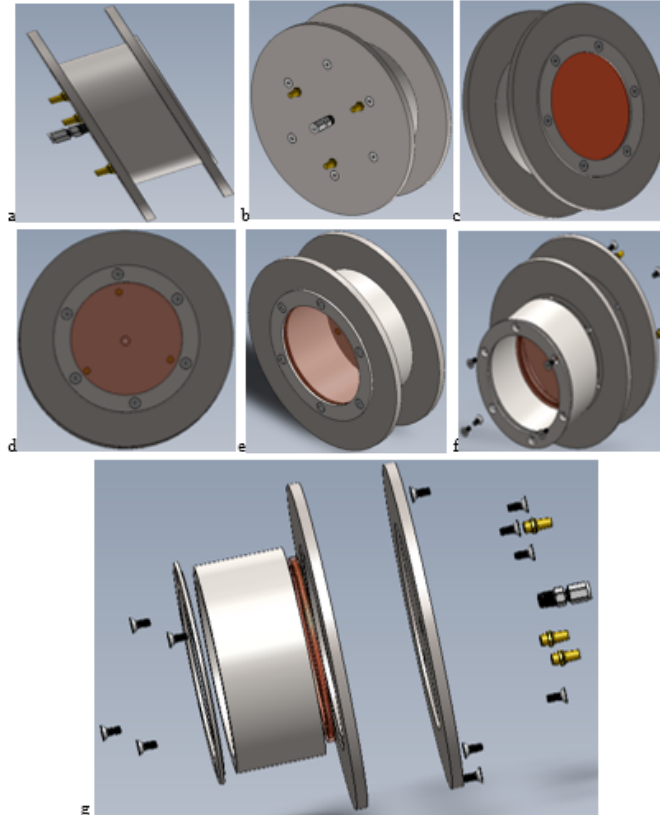


*Figure 2.* Rotary drum design. a) Side view. b) Lateral view of air inlet port. c) Lateral view of sapphire window. d) Lateral view of quartz window with air inlet and outlet holes. e) Lateral view of the sapphire window. f) Lateral view of an exploded drum with stainless steel core and titanium wheels. g) Side view of exploded drum.

Quartz is used as a window material due to its mechanical strength, chemical resistance, and low thermal expansion coefficient. One major disadvantage to quartz in this application is its optical transmission window. It only transmits energy up to the near-infrared spectrum. The infrared camera cannot see through quartz because the infrared waves cannot pass through it. A sapphire window is installed on the camera-facing side of the rotary drum due to its transmission range of 150 nm – 4.5  $\mu\text{m}$  (Optical Substrates, 2018).

Three different quartz windows were used in this study. One quartz window, pictured below in Figure 3, features a central inlet hole for hot air to be forced into the drum for internal heating. It also has four smaller holes around the edge and 11 holes extending radially from the center that are used for thermocouple temperature measurement, if desired.

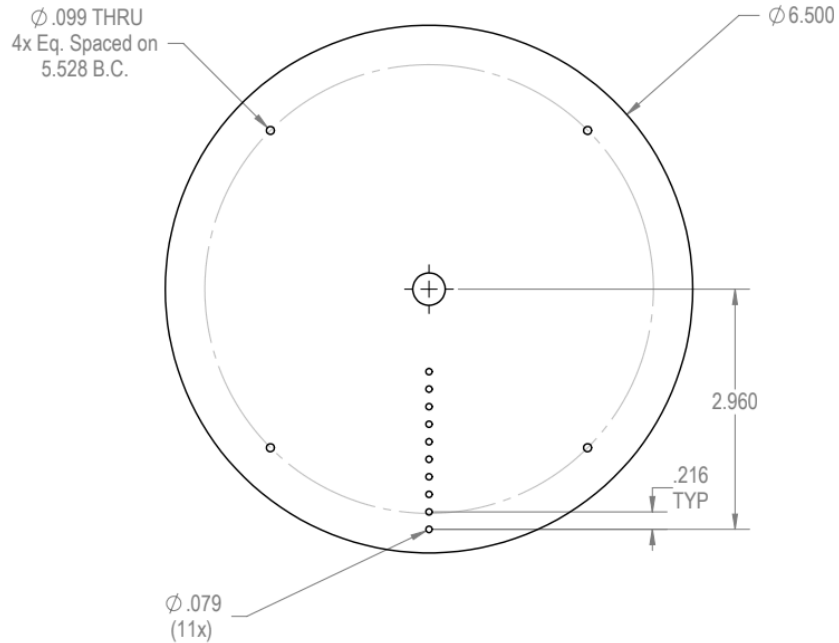


Figure 3. Quartz window specifications with air inlet hole in the center. All dimensions are in inches.

The other two quartz windows were designed without the central air inlet hole. One of them also has the 11 holes extending radially from the center, and the other does not. Both of these windows were designed for use when the drum is only heated via the external drum wall.

### Auxiliary Materials

The particles of interest in this study are soda-lime-silica glass beads. Silica is a common catalyst support material, so a good understanding of its heat transfer properties

will help improve its operating efficiencies (Chaudhuri et al., 2010). The beads are 3 mm in diameter with 90 % sphericity and a thermal conductivity of 0.7 – 1.3 W/(mK), from Potters Industries.

The drum rests on two stainless steel rods controlled by a motor with a maximum rotation rate of 11 rpm. The rotation rate and direction are adjusted with a control knob.

Four heat guns are used to heat the drum externally and internally. Three external heat guns are positioned equidistantly around the drum and heat the drum wall for conductive heating to the particle bed inside the drum. The internal heat gun is attached to an air duct that connects with pipe fittings to a temperature sensor and the air inlet port. This heat gun serves to insert a hot air stream into the drum to heat the particle bed inside via forced convection. Heat gun settings are given below in Table 2.

Table 2

*Heat gun settings.*

	Temperature (°F)	Flow rate (cfm)
3x External heat gun	600	17.6
1x Internal heat gun*	300	10.6

\*The internal heat gun is only used in the experiments involving forced convection.

A FLIR A6700SC infrared camera is used for continuous, noninvasive temperature measurement. Data from the camera is recorded in the FLIR ResearchIR software, which allows for real-time viewing and post-processing data analysis. The camera measures electromagnetic radiation, so natural and artificial lighting in the room can skew measurements. The experiments are performed in a completely dark environment with blackout curtains covering the windows. The entire rotary drum setup is shown below in Figure 4.

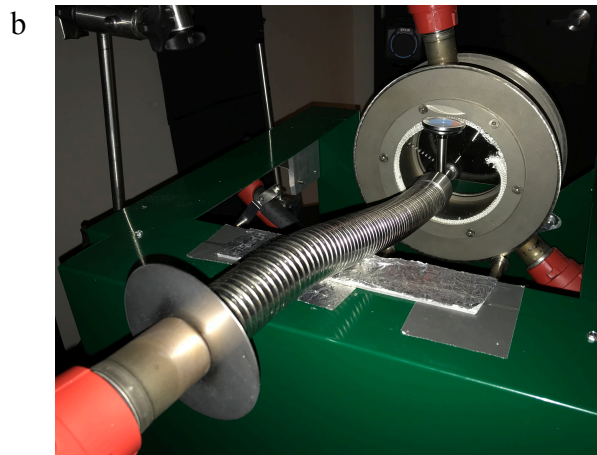
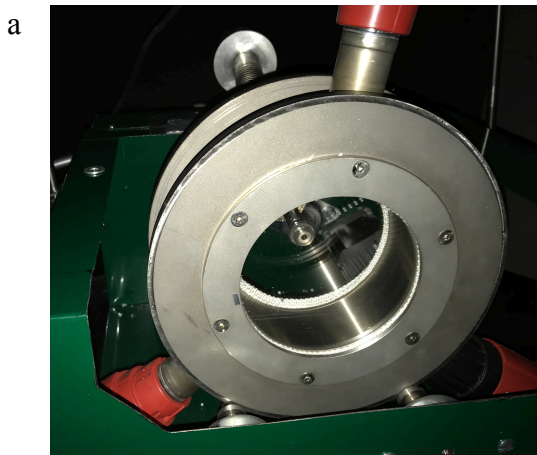


*Figure 4.* Rotary drum experimental setup. a) Front view of empty drum with sapphire window. b) Rear view of empty drum with air inlet duct and quartz window.

## CHAPTER 3

### METHODS

#### **Calibration Procedures**

The particle bed mass was calibrated for the particle size because particle beds of different particle sizes have different solids fractions. This study only involved 3 mm particles, so separate calibrations would have to be done to determine the bed mass for other particle sizes. The particles were poured into a graduated cylinder to different nominal volumes (100, 150, 200, and 250 mL) to determine the solids fraction. The particles at each nominal volume were massed, and the actual particle volume was calculated using the density of silica. The solids fraction was calculated as the ratio of the measured volume to the nominal volume. Then, the mass for each fill level was calculated using Equation A1.

To gather accurate temperature data over a temperature range of 24 – 200 °C, the infrared camera had to be manually calibrated for both the silica particles and the inner drum wall. The infrared camera outputs signals, referred to as “counts,” for each energy input it receives. The counts value is stored as a 14-bit number, so it has a range of 0 to 16383 (FLIR, 2016). This is why there are separate temperature range options in the software. For example, when beginning an experiment in the 10 – 90 °C range, the counts value will increase until it approaches 16383 at 90 °C, at which point the camera is “out of range,” and cannot interpret the data. This problem is easily avoided by monitoring the temperature throughout the experiment and selecting a higher temperature range. Each camera range must be calibrated to temperature values.

The particle temperature was calibrated by measuring the temperature of a heated particle using thermocouples and comparing those temperature values to the counts values from the infrared camera. A 3 mm particle was heated on a hot plate behind the drum window. It was held in place by a washer and three thermocouples as shown in Figure 5.

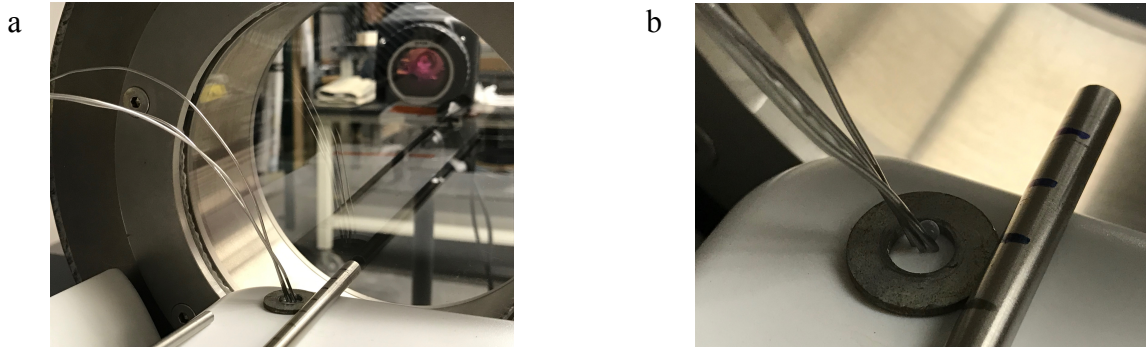


*Figure 5.* Particle calibration setup. a) Side-view showing the infrared camera and hot plate. b) Close-up view of particle resting between three thermocouples.

The particle was heated to cover all temperature values within the 10 – 90 °C, 35 – 150 °C, and 80 – 200 °C ranges. The 80 – 200 °C range, however, only included data up to 160 °C since that was the maximum temperature achieved with the hot plate. The thermocouple temperatures were averaged and plotted as a function of the infrared counts value. A polynomial trend line was fit to each temperature range to create the calibration curves shown in Figure A2.

A similar calibration was done for the inner drum wall temperature. The drum was placed on the rollers with both windows on and no particles inside. Two thermocouples were positioned on the wall at the same spot the data was collected from the experiments to prevent any error due to variations in the angle from the camera to the wall. All three heat guns were pointed at this spot on the exterior of the drum wall to

allow the inner wall to quickly heat to 200 °C. This setup is shown below in Figure 6 and the corresponding calibration curves are shown in Figure A3.

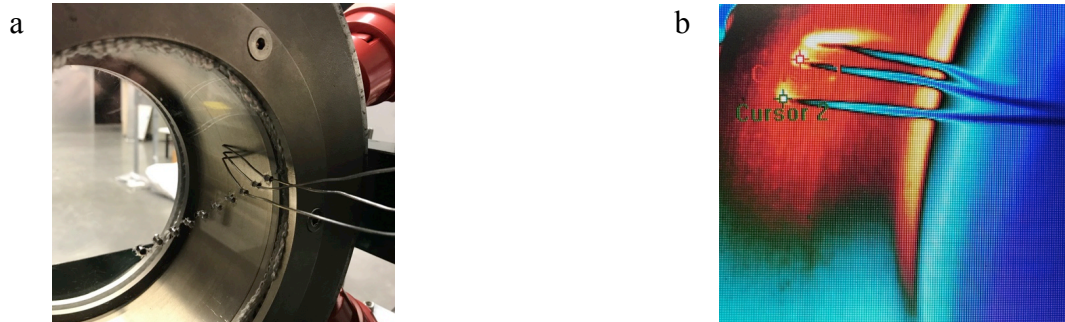


*Figure 6.* Wall calibration setup. a) View of thermocouples entering the drum through the quartz window. b) Infrared camera view of the thermocouples touching the inner drum wall.

The camera tripod was always positioned at the same spot on the ground, which was marked with tape to ensure consistency between runs. The position that offered the optimal field of view of the inner drum wall and particle bed was achieved by placing the camera lens about 65 cm away from the drum. Although the camera was always placed at this position, the effect of distance on the infrared counts value was measured in a final calibration study. The same setup shown in Figure 5 was used to heat a single particle. The metal bar on the hot plate was used to measure the distance beyond the window in cm. The camera was then moved over a distance of 40 to 100 cm away from the particle to measure the counts. This was done at 50 and 100 °C and the corresponding data is shown in Figure A4. It was determined that the distance from the camera lens to the measured object does not affect the infrared counts value in the range of 40 to 100 cm.



## Experimental Procedures

Two sets of experiments were completed to study the effects of conduction and convection in the rotary drum. These will be described as Case 1 and Case 2 for simplicity throughout the rest of this paper and both setups are pictured in Figure 7.

Case 1. Conduction only, using only external heat sources. These experiments used three heat guns to heat the exterior drum wall.

Case 2. Conduction with convection, using external and internal heat sources. These experiments used one heat gun to supply hot air to the inside of the drum in addition to the three heat guns for heating the exterior drum wall.

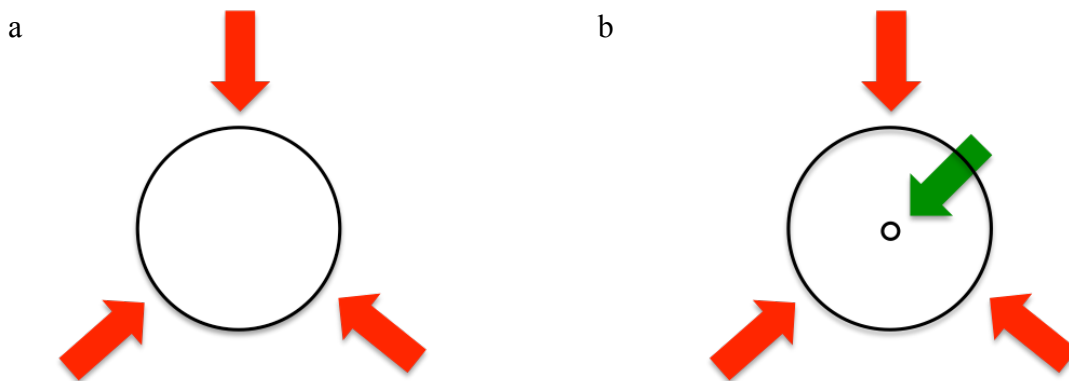


*Figure 7.* Schematic of the two experimental setups used. a) Case 1: conduction only, using only external (red) heat sources. b) Case 2: conduction with convection, using external (red) and internal (green) heat sources.

In both cases, dry particles were weighed to the desired fill level and placed inside the drum. The quartz window was secured in place with the titanium plate and bolts, and then the drum was placed on the rollers. The rotation motor was started at the desired rotation rate, and the heat guns were turned on. The infrared camera recording was started and the experiment was run until the average particle bed temperature reached steady state. As the system temperature increased, the camera temperature range was switched in

the ResearchIR software from 10 – 90 °C to 35 – 150 °C, and then to 80 – 200 °C. The frame number for each range transition was recorded so the applicable calibration curve could be applied during data analysis. Once the average particle bed temperature reached steady state, the recording was stopped and the heat guns and rotation were turned off. The drum was removed for disassembly, emptied, and left to cool for the next run. The particles were rinsed with water to remove any dust or particulate contaminants and left to dry overnight. The conduction experiments used different particles than the convection experiments, but both sets of particles were from the same manufacturer batch of 3 mm silica beads.

### **Design of Experiments**

This study employed a three level, two factor, full factorial design of experiments (DOE) with two replicates to determine the effects of fill level and rotation rate on the average wall-particle heat transfer coefficient. Randomized DOEs were completed for both Case 1 and Case 2. Each DOE had 27 runs, for a total of 54 runs. The parameters for each run in Case 1 and Case 2 are shown below in Table 3.

Table 3

*Full factorial DOE with randomized run order for Case 1 and Case 2.*

Run	Case 1		Case 2	
	Fill Level (%)	Rotation Rate (rpm)	Fill Level (%)	Rotation Rate (rpm)
1	17.5	10	10	10
2	10	2	10	2
3	25	6	25	10
4	17.5	2	10	2
5	17.5	2	25	2
6	10	10	25	10
7	25	10	10	10
8	25	10	25	2
9	17.5	2	10	6
10	10	10	25	6
11	17.5	10	17.5	2
12	25	2	17.5	6
13	25	6	17.5	10
14	17.5	10	17.5	2
15	17.5	6	17.5	6
16	10	2	17.5	10
17	10	6	10	6
18	17.5	6	25	6
19	25	2	10	2
20	17.5	6	25	6
21	25	6	17.5	6
22	10	6	10	10
23	10	10	25	2
24	10	6	17.5	10
25	25	10	17.5	2
26	10	2	10	6
27*	25	2	25	10

\*The last run in the Case 1 DOE was not completed due to issues with the drum rollers; there is only 1 replicate for the run with 25 % fill level and 2 rpm.

## Analytical Procedures

The ResearchIR software allows the user to select a “region of interest” (ROI) to view and export data for that region. An ROI was drawn on the inner drum wall and around the particle bed as shown below in Figure 8.

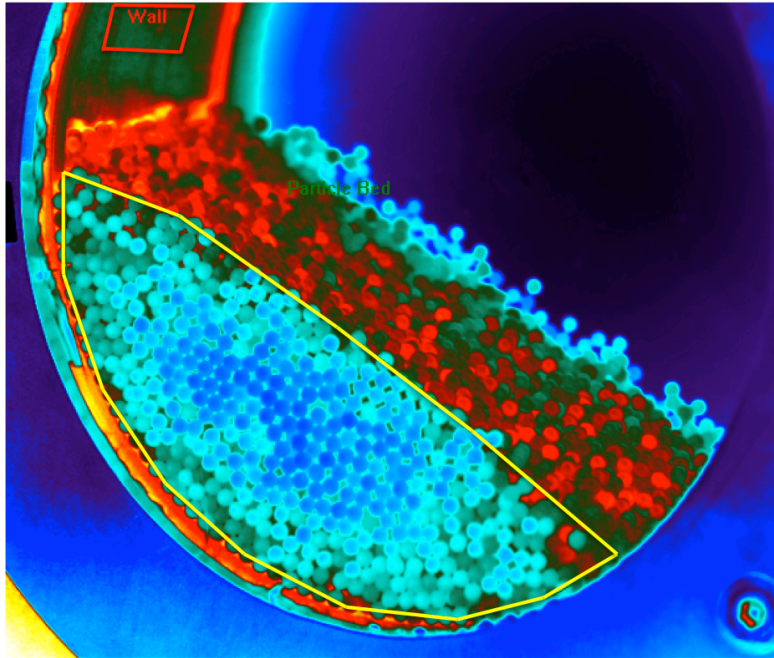


*Figure 8.* Region of interest selection for the drum wall (red) and particle bed (yellow) in the ResearchIR software. This is an example for a 25 % fill level, 10 rpm run.

The data were exported as counts values into a MATLAB script, shown in Appendix A. The script applied the appropriate calibration curves to convert the counts data to temperature data. It also applied the constants from Equation 4 to calculate the heat transfer coefficient, using the slope of the natural log of the normalized particle bed temperature versus time. This slope was constant until the average particle bed temperature reached a steady state, so only the first few minutes of data was needed. For this reason, the analysis was only performed up to the transition from the 10 – 90 °C range to the 35 – 150 °C range.

## CHAPTER 4

### RESULTS AND DISCUSSION

#### Flow Profile

The theoretical flow profile predicted by Mellman (2001) was determined for each run using the Froude number,  $Fr$ , and fill level. The flow profile was observed during each run and recorded. These results are shown below in Table 4.

Table 4

*Observed and theoretical flow profiles based on  $Fr$  and Table 1.*

Fill %, rpm	$Fr$ ( $\times 10^4$ )	Theoretical Flow Profile	Observed Flow Profile	
			Case 1	Case 2
10 %, 2 rpm	3.4	Rolling/Slumping	Slumping/Surgings	Slumping
10 %, 6 rpm	31	Rolling/Slumping	Slumping/Surgings	Slumping
10 %, 10 rpm	85	Rolling	Rolling/Slumping/Surgings	Rolling
17.5 %, 2 rpm	3.4	Rolling	Slumping/Surgings	Slumping
17.5 %, 6 rpm	31	Cascading/Rolling	Slumping/Surgings	Slumping
17.5 %, 10 rpm	85	Cascading/Rolling	Rolling/Slumping	Rolling
25 %, 2 rpm	3.4	Rolling	Rolling/Slumping/Surgings	Rolling
25 %, 6 rpm	31	Cascading/Rolling	Rolling/Slumping/Surgings	Rolling
25 %, 10 rpm	85	Cascading/Rolling	Rolling/Slumping	Rolling

Some runs have more than 1 theoretical flow profile because each flow regime has a wide range of potential  $Fr$  and fill levels. At least two flow profiles were observed for every run in Case 1, while only one flow profile was observed for each run in Case 2. The initial flow profile observed for each Case 1 run matched the flow profile observed for the corresponding Case 2 run. As the particles heated in Case 1, particle-particle friction took over and inhibited the bed movement, causing a transition from the initially observed flow profile. This is because the friction coefficient increases as temperature increases (Lenard, J.G. & Kalpakjian, S., 1991). In Case 2, the particles were in the

presence of the hot inlet air stream. This air into the drum effectively fluidized the particle bed so that the fluidization velocity dominated the friction coefficient. In this case, the particle bed followed the same flow profile throughout each run as temperature increased.

The surging regime should not be possible at rotation rates greater than 2 rpm according to Table 1, based on the calculated  $Fr$ . However, surging flow was observed for nearly every run in Case 1 due to the particle-particle friction dominating the wall-particle friction. Once the bed began surging, the particles within the bed were no longer mixing together. Instead, the bed moved as one mass, oscillating back and forth along the drum wall. Cascading flow was never observed, although some of the calculated  $Fr$  did lie in the cascading regime. Discrepancies such as this between the theoretical and observed flow profiles are attributed to the assumptions under which Mellman (2001) developed the flow profiles. He only considered the frictional effects between the wall and particle bed. Although, the experimental observations suggest that particle-particle friction dominated when the particle bed was heated.

### **Wall-Particle Heat Transfer Coefficient**

For the analysis of the heat transfer coefficient, it must be noted that the original quartz window broke during the Case 1 DOE on run 14 out of 27. All 27 runs for Case 2, and the first 14 runs for Case 1 were performed using a quartz window with 11 thermocouple holes extending radially from the center (Figure 3). Run 15 through 27 for the Case 1 DOE were performed using a quartz window with no holes since this was the only other window available. The data from the Case 1 experiments were split into two

categories: Case 1 – holes, representing the experiments using the window with holes, and Case 1 – no holes, representing the experiments using the window without holes.

Figure 9 shows the average wall-particle heat transfer coefficient for each set of fill levels and rotation rates. The error bars represent +/- one standard deviation from the mean for each set of three trials. Some of the data sets are missing values for the heat transfer coefficient due to the randomized run order in the DOE. For example, all three trials for the Case 1 experiments at 17.5 % fill level and 6 rpm were performed after run 14, using the window without holes; so there is no data to report for this set using the window with holes. This is also why some of the sets are missing error bars; in those cases, there was only one trial done using that window. Additionally, some of the sets that do have error bars present a large range of error since there is more variation from the mean with less data in each set. The analytical procedure also contributed to the error because new ROIs were drawn for each trial. Large error bars are expected in these experiments due to the unconventional nature of particulate systems and the amount of data manipulation done to determine the heat transfer coefficient for each run. Despite the sources of error, there are plenty of conclusions to draw from the effects of fill level and rotation rate in each case.

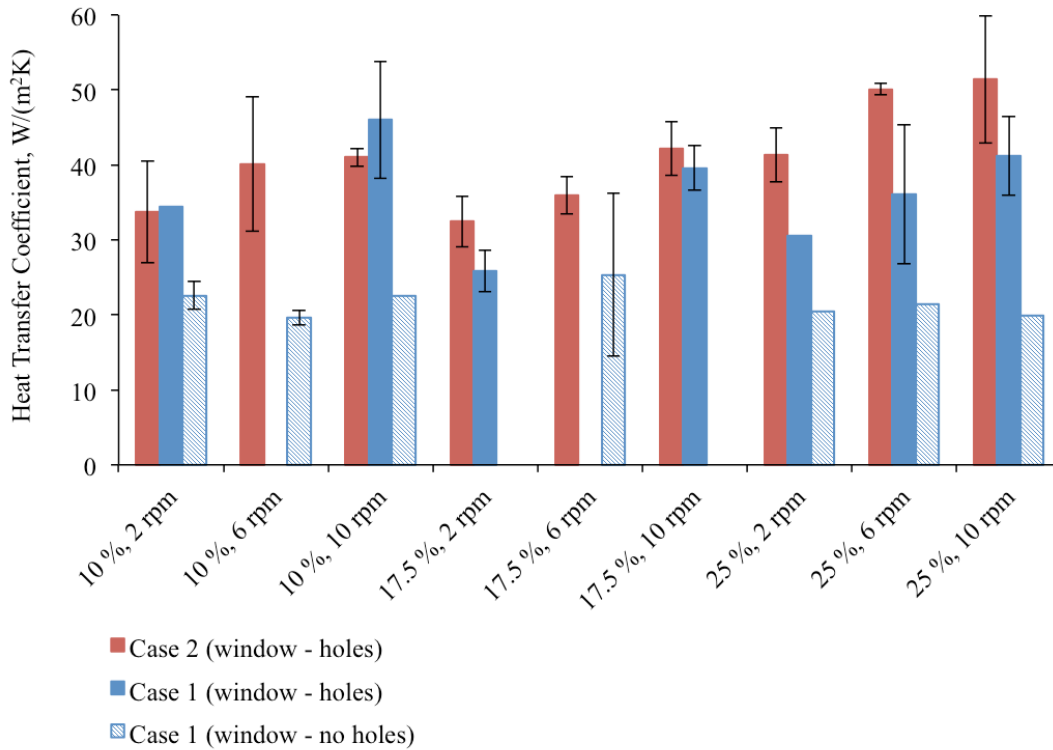


Figure 9. Average wall-particle heat transfer coefficient for each combination of fill level and rotation rate.

Although unplanned, the unfortunate window breakage offered some insight into a factor that was not previously considered. The presence of the thermocouple holes was originally considered negligible since the combined area of all 11 holes only accounts for 0.16 % of the surface area of the quartz window. This effect was found to be significant due to the substantial difference in the heat transfer coefficient between the Case 1 data for the window with holes compared to without holes. In every set, the window without holes yielded a smaller heat transfer coefficient than the window with holes. If the holes allow heat to escape the drum quicker, then the lack of holes traps heat inside the drum. This phenomenon drives the wall temperature higher because less heat is lost from the drum wall to the atmosphere through the holes in the window. Since stainless steel has a



larger thermal conductivity than silica, the drum wall tends to lose heat via convection more quickly than the particle bed. When the heat loss is minimized due to the lack of holes in the window, the wall temperature increases and drives the wall-particle temperature gradient to larger values, decreasing the heat transfer coefficient.

To compare the effects of fill level and rotation rate, only the data for the window with holes is considered. For a constant fill level, increasing the rotation rate increased the heat transfer coefficient in both Case 1 and Case 2. This confirms the expectation that a rolling bed increases the heat transfer between the drum wall and particle bed by increasing the number of wall-particle and particle-particle contacts. The effect of fill level at a constant rotation rate is not as significant. Although there is less mass and therefore less resistance to heating the particle bed at lower fill levels, the hydrodynamics are impeded since the bed tends to the slumping or surging regime. At low fill levels, the effect of convection is also minimized. Convection has a larger impact on the heat transfer coefficient as the fill level increases, indicated by the increasing separation between the red and blue bars in Figure 9. This is due to the larger surface area achieved with a larger particle bed. Not only is the exposed surface larger, the total bed surface area also increases since the hot air penetrates the interstitial spaces between particles.

Figure 10 shows the heat transfer coefficient for Case 2 for each fill level and rotation rate. This contour plot demonstrates the increasing impact of convection at higher fill levels for a constant rotation rate. The wall-particle heat transfer coefficient was maximized at 25 % fill level and 10 rpm because the surface area for heat transfer was largest and the flow profile was rolling, maximizing the wall-particle and particle-particle contacts.

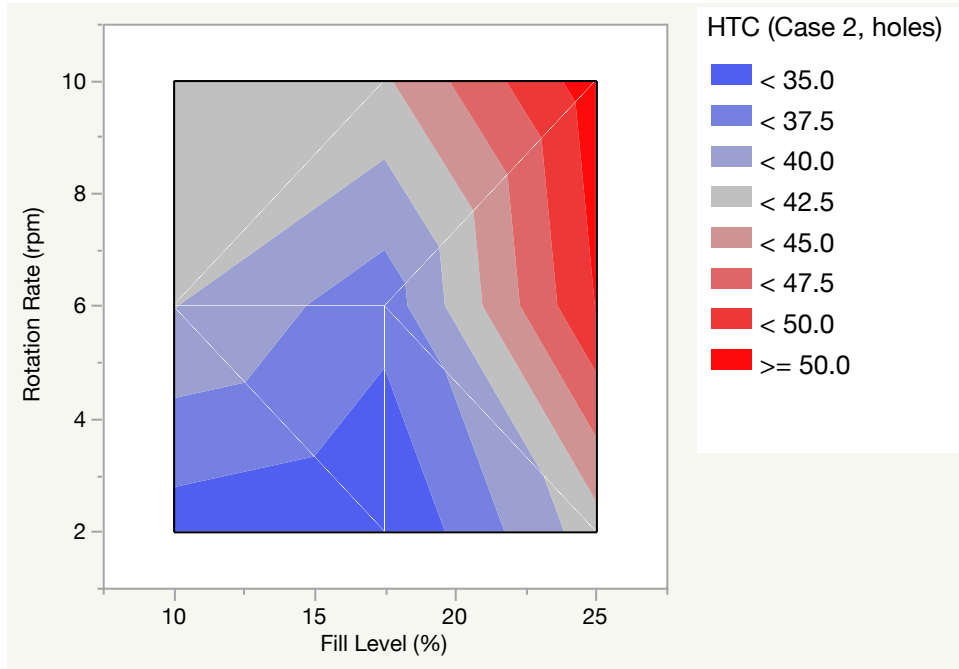


*Figure 10.* Contour plot of the average wall-particle heat transfer coefficient (HTC) as a function of fill level and rotation rate for Case 2, using the window with holes. HTC units are  $W/(m^2K)$ .

The contour plot in Figure 11 presents the heat transfer coefficient for Case 1, using the window with holes. Increasing the fill level had competing effects of improving the hydrodynamics, but also increasing the resistance to heat transfer due to the larger bed mass. For a constant rotation rate, this caused the heat transfer coefficient to increase as fill level increased from 10 % to 17.5 %, and decrease as fill level increased from 17.5 % to 25 %. Rotation rate was more significant than fill level in this case because there was no forced convection into the drum. The dominant heat transfer mechanism, in this case, was contact conduction, which increased as the rotation rate increased. The heat transfer coefficient was maximized at 10 % fill level and 10 rpm. These results corroborate the findings of Nguyen et al. (2015), Emady et al. (2016), and Njeng et al. (2018).

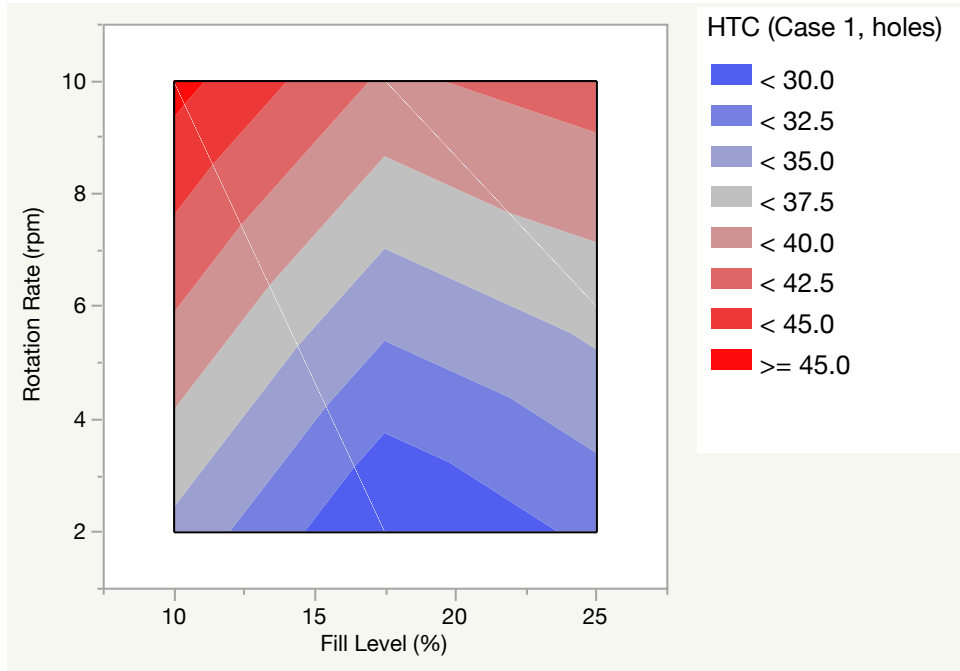
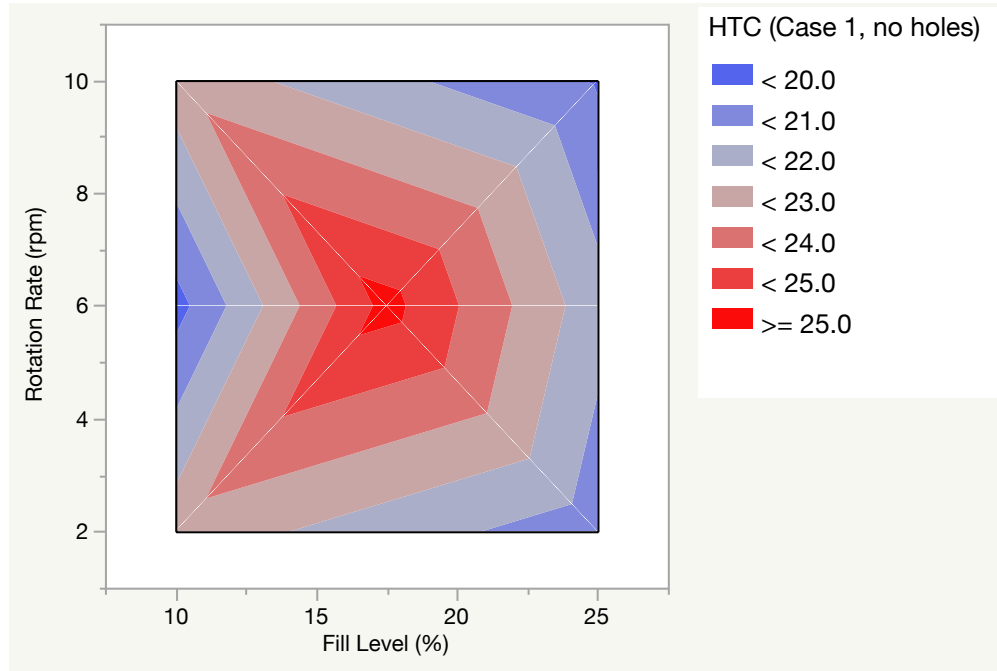


Figure 11. Contour plot of the average wall-particle heat transfer coefficient (HTC) as a function of fill level and rotation rate for Case 1, using the window with holes. HTC units are  $W/(m^2K)$ .

Figure 12 displays the heat transfer coefficient for Case 1, using the window without holes. In this case, the fill level and rotation rate had nearly an equal effect on the heat transfer coefficient. There was less heat loss due to the lack of holes in the window, so the temperature gradient between the wall and particle bed was maximized since the wall did not lose heat as quickly to the air as it did with the window with holes. This suggests that the heat loss using the window with holes was significant. Using the window without holes, the heat transfer coefficient appeared largest at 17.5 % fill level and 6 rpm. However, the scale in Figure 12 only has a range of 5  $W/(m^2K)$ , compared to 15  $W/(m^2K)$  in Figures 10 and 11. Most of the error bars' magnitudes are larger than 5  $W/(m^2K)$ . Therefore, neither fill level nor rotation rate significantly impacted the heat transfer using the window without holes.



*Figure 12.* Contour plot of the average wall-particle heat transfer coefficient (HTC) as a function of fill level and rotation rate for Case 1, using the window without holes. HTC units are  $W/(m^2K)$ .

### Fluid-Particle Heat Transfer Coefficient

The procedure outlined in Equations 5 – 7 was followed to calculate the fluid-particle heat transfer coefficient due to forced convection by the rotation of the drum wall in a closed system (Shi et al., 2008). The maximum value for  $h_f$  was  $2.7 W/(m^2K)$  at 10 rpm. This was close to the values found by Shi et al. (2008) and Debacq et al. (2011). A fluid-particle heat transfer coefficient of  $2.7 W/(m^2K)$  is more than an order of magnitude smaller than the wall-particle heat transfer coefficient in each case. This suggests that the heat loss was not driven by the forced convection due to the wall rotation, but rather by natural convection due to the temperature gradient between the air inside the drum and the air outside the drum.

The Biot number was calculated using Equation 8 to show that no temperature gradient existed within every single particle. Using the maximum value for  $h_f$  of 2.7 W/(m<sup>2</sup>K), the Biot number was calculated to be less than 0.004. This is much less than 1, indicating internal conductive resistance was lower than external convective resistance, so each particle had a uniform temperature.

## CHAPTER 5

### CONCLUSION AND FUTURE WORK

#### **Conclusion**

This research investigated the effects of fill level and rotation rate on the particle bed hydrodynamics and the wall-particle heat transfer coefficient, using 3 mm silica beads in a stainless steel rotary drum. The stainless steel drum core has an ID of 6 in., a length of 3 in., and is supported by two 11 in. titanium wheels to protect and insulate the drum. A quartz window and a sapphire window cap the ends of the drum. Temperature data was gathered using an infrared camera aimed through the sapphire window. Two full factorial DOEs were completed to understand the contributions of conduction and convection at fill levels of 10 %, 17.5 %, and 25 %, and rotation rates of 2 rpm, 6 rpm, and 10 rpm. Two replicates were performed for error analysis, so each DOE had 27 runs, for a total of 54 runs. Case 1 used only external heating, so the drum system was assumed closed with no moving fluid and heat transferred from the wall to particle bed via conduction. Case 2 used external and internal heating to introduce forced convection to the system. The original quartz window with 11 thermocouple holes that was used for all 27 Case 2 runs and runs 1-14 of Case 1, broke during run 14 of Case 1. A new quartz window with no holes was used for runs 15-26 of Case 1.

Case 1 and Case 2 initially exhibited the same flow profile, but in Case 1 the particle bed stagnated as the particles heated and particle-particle friction increased. The contributions of convection on the wall-particle heat transfer coefficient increased as the fill level increased due to the additional surface area available for particle-fluid contact. In Case 1, using the window with holes, the heat transfer coefficient was maximized at a

high rotation rate and low fill level. The window without holes decreased the heat loss from the system, which decreased the heat transfer coefficient by increasing the wall-particle temperature gradient. Fluid-particle forced convection was found to be negligible in the closed system of Case 1, suggesting that heat loss from the system was dominated by natural convection due to the temperature gradient between the drum contents and external environment. These findings provide a new method for studying the heat transfer in rotary drum systems and contribute to increasing operating efficiencies and energy savings on a global scale.

### **Future Work**

To fill the data gap created by the broken quartz window, new windows should be purchased to complete the originally planned DOE and produce error bars for each set. Future studies should include radiation heat transfer to understand its effects on the flow profile and heat transfer coefficient. Additionally, more experiments should be done studying forced convection at varying inlet air temperatures and flow rates. Studying materials other than silica at varying particle size distributions would provide more knowledge of the flow profile transitions at elevated temperatures. To better understand the heat transfer mechanisms in the rotary drum system, shorter experiments should be run while recording at a higher frame rate to quantify localized wall-particle and particle-particle heat fluxes.

## REFERENCES

- Chaudhuri, B., Muzzio, F.J., Tomassone, M.S. (2010). Experimentally validated computations of heat transfer in granular materials in rotary calciners. *Powder Technology*, 198, 6-15.
- Debacq, M., Thammavong, P., Vitu, S., Dupoizat, M. (2011). Experimental apparatus for studying heat transfer in externally heated rotary kilns. *Chemical Engineering Technology*, 34, 707-717.
- Emady, H.N., Anderson, K.V., Borghard, W.G., Muzzio, F.J., Glasser, B.J., Cuitino, A. (2016). Prediction of conductive heating time scales of particles in a rotary drum. *Chemical Engineering Science*, 152, 45-54.
- FLIR. (August 19, 2016). ResearchIR 4 User's Guide.
- International Energy Agency. (January 25, 2019). Cement. Retrieved March 25, 2019, from <https://www.iea.org/tcep/industry/cement/>.
- Lenard, J.G., Kalpakjian, S. (1991). The effect of temperature on the coefficient of friction in flat rolling. *CIRP Annals*, 40, 223-226.
- Lueptow, R.M., Akonur, A., Shinbrot, T. (2000). PIV for granular flows. *Experiments in Fluids*, 28, 183-186.
- Mellman, J. (2001). The transverse motion of solids in rotating cylinders – Forms of motion and transition behavior. *Powder Technology*, 118, 251-270.
- Musser, J. (2011). *Modeling of heat transfer and reactive chemistry for particles in gas-solid flow utilizing continuum-discrete methodology (CDM)* (Ph.D. Thesis), West Virginia University, Morgantown, United States.
- Nguyen, H.T., Cosson, B., Lacrampe, M.F., Krawczak, P. (2015). Numerical simulation on the flow and heat transfer of polymer powder in rotational molding. *International Journal of Material Forming*, 8, 423-438.
- Njeng, A.S.B., Vitu, S., Clause, M., Dirion, J.L, Debacq, M. (2018). Wall-to-solid heat transfer coefficient in flighted rotary kilns: Experimental determination and modeling. *Experimental Thermal and Fluid Science*, 91, 197-213.
- Optical Substrates. (n.d.). Retrieved March 30, 2018, from [https://www.thorlabs.com/newgrouppage9.cfm?objectgroup\\_id=6973](https://www.thorlabs.com/newgrouppage9.cfm?objectgroup_id=6973).



- Oschmann, T., Kruggel-Emden, H. (2018). A novel method for the calculation of particle heat conduction and resolved 3D wall heat transfer for the CFD/DEM approach. *Powder Technology*, 338, 289-303.
- Rhodes, M. (2008). *Introduction to particle technology* (2<sup>nd</sup> ed.). John Wiley & Sons.
- Rotary Dryers. (n.d.). Retrieved April 2, 2018, from <https://appliedchemical.com/equipment/rotary-drums/rotary-dryers/>.
- Shi, D., Vargas, W.L., McCarthy, J.J. (2008). Heat transfer in rotary kilns with interstitial gases. *Chemical Engineering Science*, 63, 4506-4516.
- The Process for Making Portland Cement. (n.d.). Retrieved September 24, 2018, from <http://www.concretealberta.ca/the-process-for-making-portland-cement>.
- Wes, G.W.J., Drinkenburg, A.A.H., Stemerding, S. (1976). Heat transfer in a horizontal rotary drum reactor. *Powder Technology*, 13, 185-192.

APPENDIX A  
CALCULATIONS

### Calibration: Particle Bed Mass

The mass required for each fill level was calculated using Equation A1.

$$Mass = \phi \rho_p \pi R^2 L F \quad (A1)$$

where  $\phi$  is the solids fraction,  $\rho_p$  is the particle density, and  $F$  is the fill level fraction.

Figure A1 shows the calibration curve used to determine the required mass of 3 mm silica beads at any fill level between 10 % and 25 %.

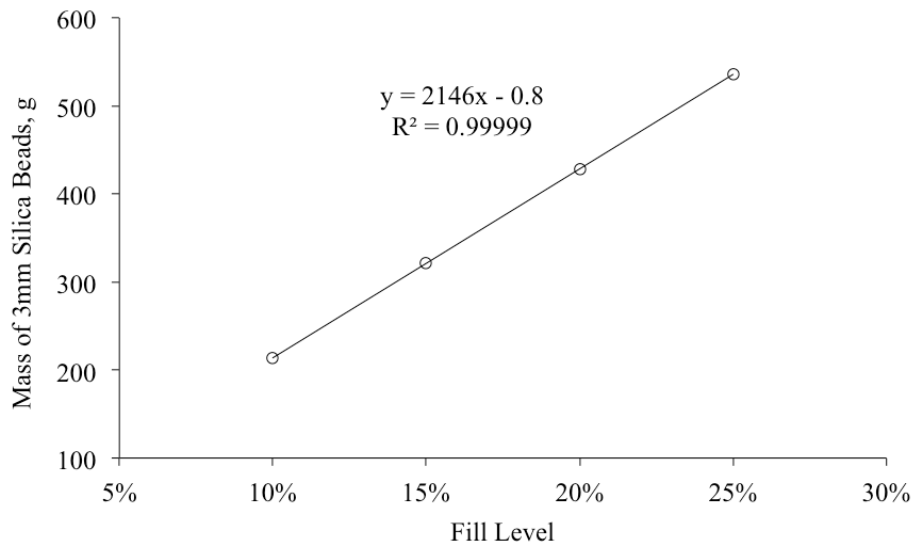


Figure A1. Mass of 3 mm silica beads required for fill levels from 10 – 25 %.

## Calibration: Particle Temperature

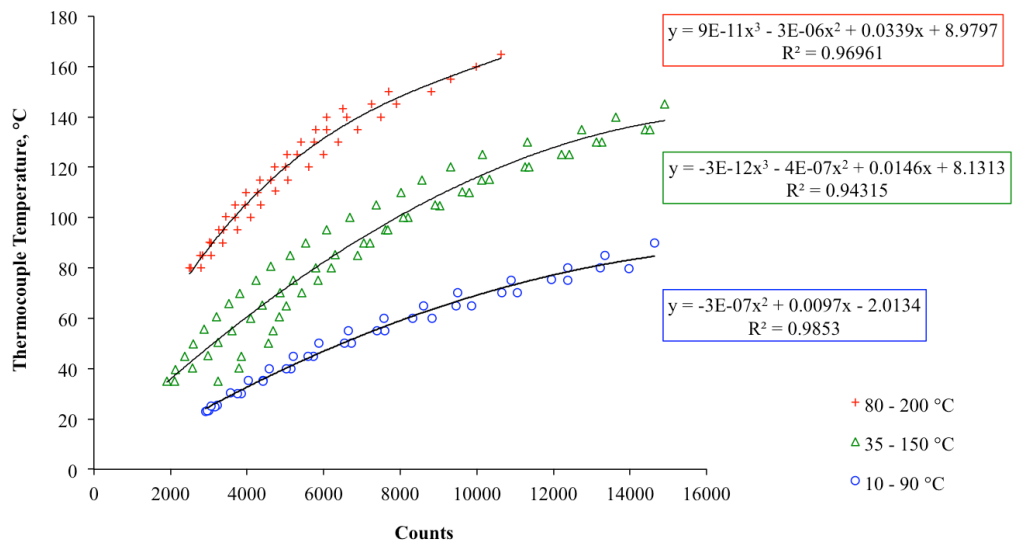


Figure A2. Particle temperature calibration curves for 10 – 90 °C, 35 – 150 °C, and 80 – 200 °C camera ranges.

## Calibration: Wall Temperature

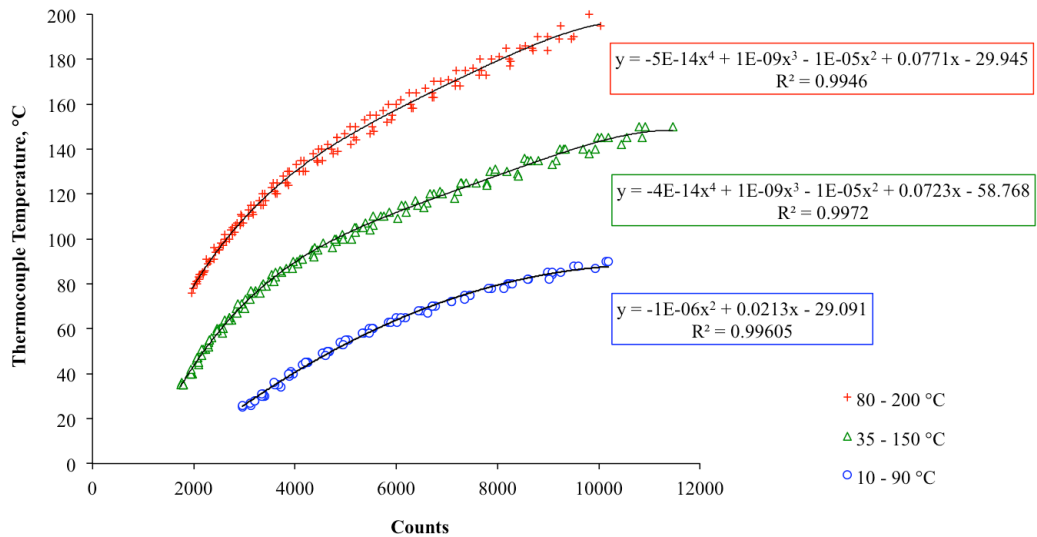


Figure A3. Wall temperature calibration curves for 10 – 90 °C, 35 – 150 °C, and 80 – 200 °C camera ranges.

### Calibration: Camera Distance

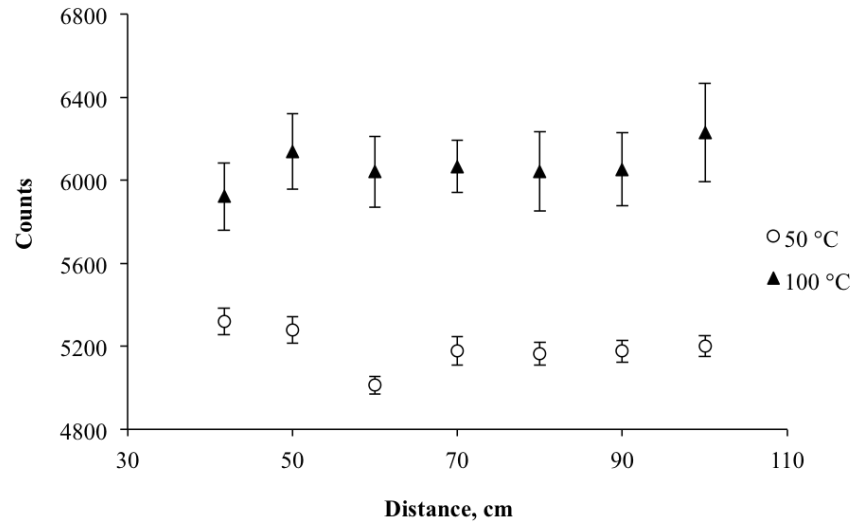


Figure A4. Infrared counts as a function of distance from object at 50 °C and 100 °C.

### Calculating $e_s$

The fraction of the drum wall touched by particles,  $e_s$ , was calculated using ImageJ software. Images of the particle bed were analyzed at each fill level and rotation rate to determine  $e_s$  for each fill level. Figure A5 below shows an example of this procedure.

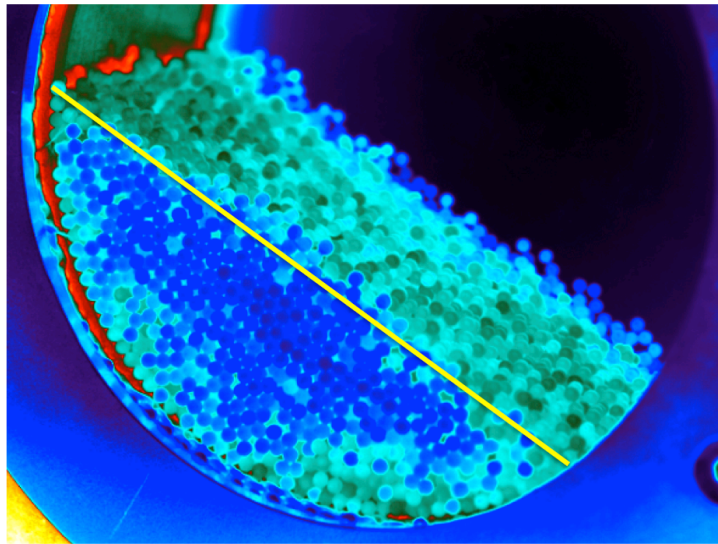


Figure A5. Image of a 25 % fill level, 10 rpm run used to determine  $e_s$ .

The yellow line in Figure A5 was drawn in ImageJ software to determine the length of the chord,  $C$ , intersecting the circle. The scale was set on the image by selecting the diameter of a particle and setting its length to 3 mm. With the length of the chord known, the arc length of the portion of the wall touched by particles was calculated. The fraction of the drum wall touched by particles is the arc length divided by the drum circumference. After simplification, the relationship between the chord length and  $e_s$  reduces to Equation A2. The  $e_s$  values found for each fill level were: 0.19 for 10 % fill, 0.25 for 17.5 % fill, and 0.28 for 25 % fill.

$$e_s = \frac{1}{\pi} \sin^{-1} \frac{C}{D} \quad (\text{A2})$$

## MATLAB Script

```
%-----%  
  
%   Variables exported from the Camera           %  
  
%   WHAT:                NAME:                %  
  
%   Frames                F                    %  
  
%   Real Time             time                 %  
  
%   Wall temperature      W_Temp              %  
  
%   Particles average temperature    P_avgTemp      %  
  
%-----%  
  
clear ; clc;  
  
datestr(clock, 0)  
  
z=cputime;  
  
%----- INPUTS -----%  
  
filename = 'filename.xlsx'; % create the file location for data  
  
Prompt1 = 'What is the fill level?';  
  
FillLevel = input(Prompt1); % fill level of the drum  
  
%-----%  
  
PI = 3.14159265;  
  
L = 0.0762 ; % drum length, m  
  
A = pi*0.1524; % drum circumference, m  
  
Cp_s = 800; % silica specific heat capacity, J/(kg*K)  
  
%----- OPEN FILE -----%  
  
% Read the second column from the Excel file %
```

```

F = xlsread(filename,'A:A');
time = xlsread(filename,'C:C');
W_Temp = xlsread(filename,'D:D');
P_avgTemp = xlsread(filename,'E:E');
F1 = length(F); %total data points

CalW_temp= zeros([F1 1]); % create an empty array for the calibrated wall temperature
CalP_temp= zeros([F1 1]); % create an empty array for the calibrated avg particle
temperature
for x=1:F1
    CalW_temp(x)=-1*10^-6*W_Temp(x).^2+0.0213*W_Temp(x)-29.091;
    % to account for the missing temperature data, replace the missing data point with
the preceding value.
    % first replace all NaN cells by 0 and then assign the value to all the zeros
    CalW_temp(isnan(CalW_temp))=0; % replaces all the NaN by a value 0
    if CalW_temp(x)==0 % if condition replaces only values that are 0
        CalW_temp(x)=CalW_temp(x-1);
    end
    CalP_temp(x)=-3*10^-7*P_avgTemp(x).^2+0.0097*P_avgTemp(x)-2.0134;
    % to account for the missing temperature data, replace the missing data point with the
preceding value.
    % first replace all NaN cells by 0 and then assign the value to all the zeros
    CalP_temp(isnan(CalP_temp))=0; % replaces all the NaN by a value 0
    if CalP_temp(x)==0

```



```

    CalP_temp(x)=CalP_temp(x-1);
end

end

Tinitial= CalP_temp(1); % set initial particle temperature
LNFUN = log((CalW_temp - CalP_temp)./(CalW_temp - Tinitial)) ;
figure(1)
plot(time,CalP_temp,'r*',time,CalW_temp,'ko')
xlabel('Time [s]')
ylabel('Temperature [°C]')
legend('Solid bed','Drum wall','Location','northwest')
p = polyfit(time, LNFUN(1:F1),1); % trendline
ln_reg = polyval(p,time(1:F1)); % linear regression curve
% assign es value based on Fill level
if (FillLevel==10)
    es=0.19;
elseif (FillLevel==17.5)
    es=0.25;
else
    es=0.28;
end

M_particle = 0.0215*FillLevel-0.0008; % derived the equation from the relationship
between fill level and mass of particles
ht_c= p(1).*-1*M_particle.*Cp_s/(es*A*L);

```

```
figure(2)
plot(time, LNFUN, '!', time, ln_reg); %ln_fun plot
xlabel('Time [s]')
ylabel('ln((T_{w}-T_{s})/(T_{w}-T_{s0})))')
txt = ['Heat Transfer Coefficient = ' num2str(ht_c) ' [W/(m^2K)]'];
text(150,-0.2,txt,'Color','red','FontSize',12)
e = cputime-z
```

APPENDIX B

RAW DATA

### Case 1 Experiments (Conduction Only)

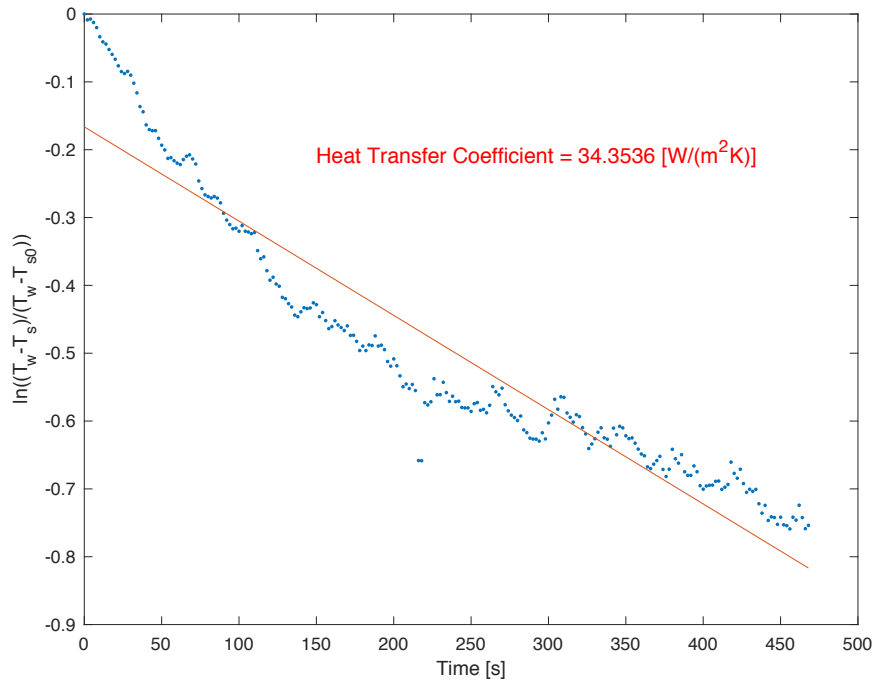


Figure B1. Case 1, 10 % fill level, 2 rpm, Trial 1.

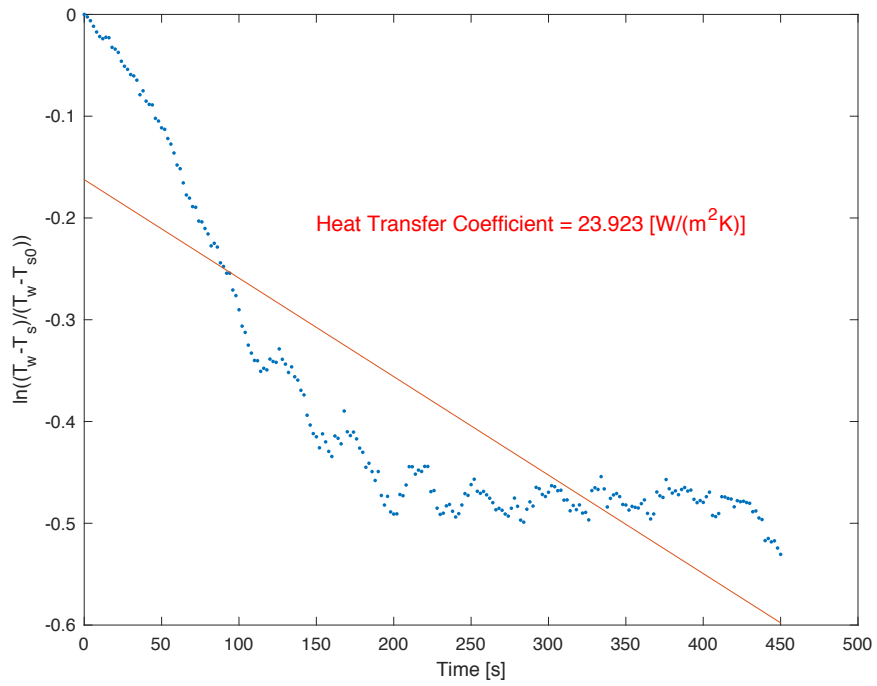


Figure B2. Case 1, 10 % fill level, 2 rpm, Trial 2.

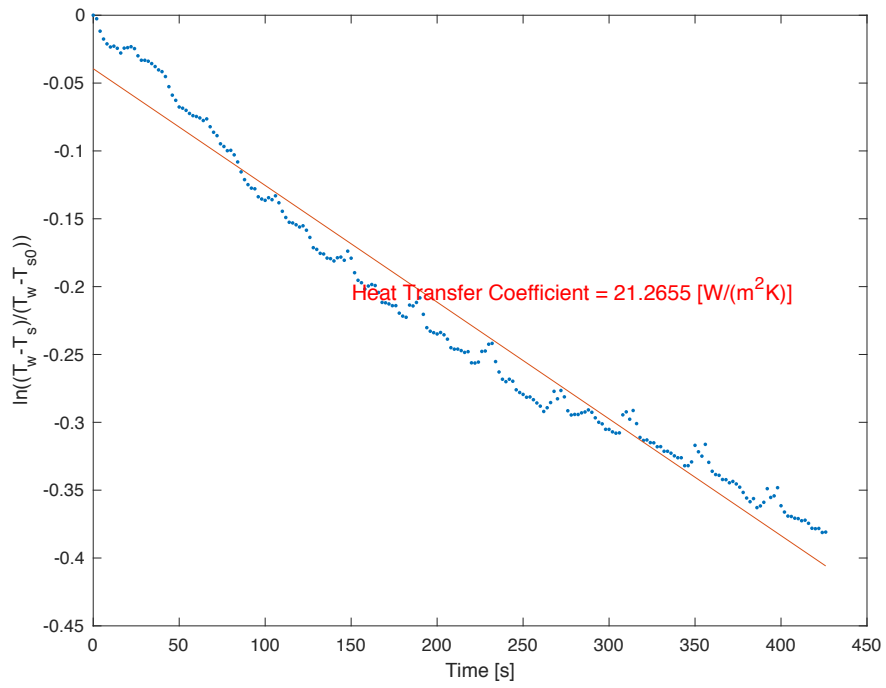


Figure B3. Case 1, 10 % fill level, 2 rpm, Trial 3.

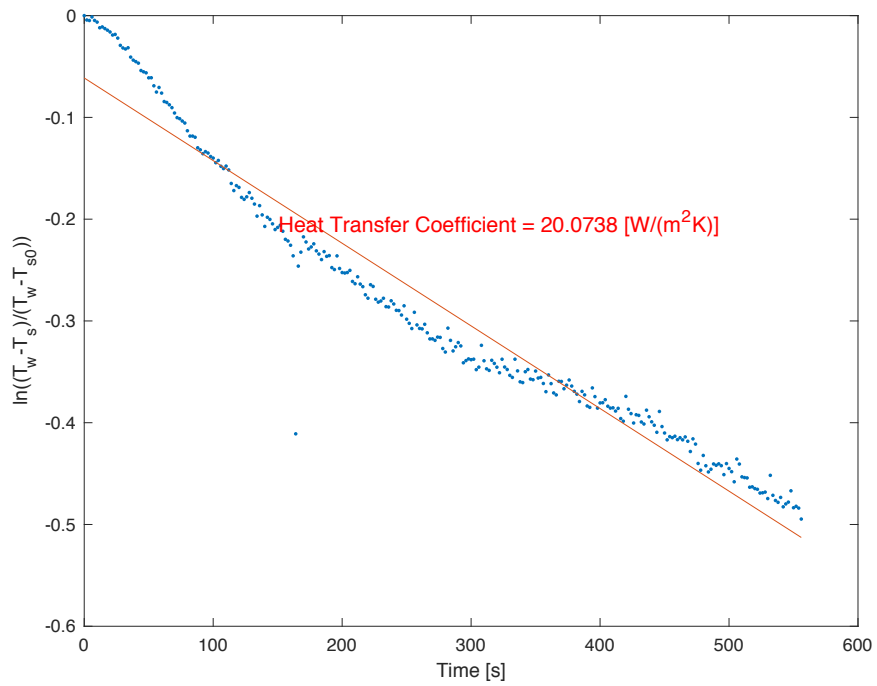


Figure B4. Case 1, 10 % fill level, 6 rpm, Trial 1.

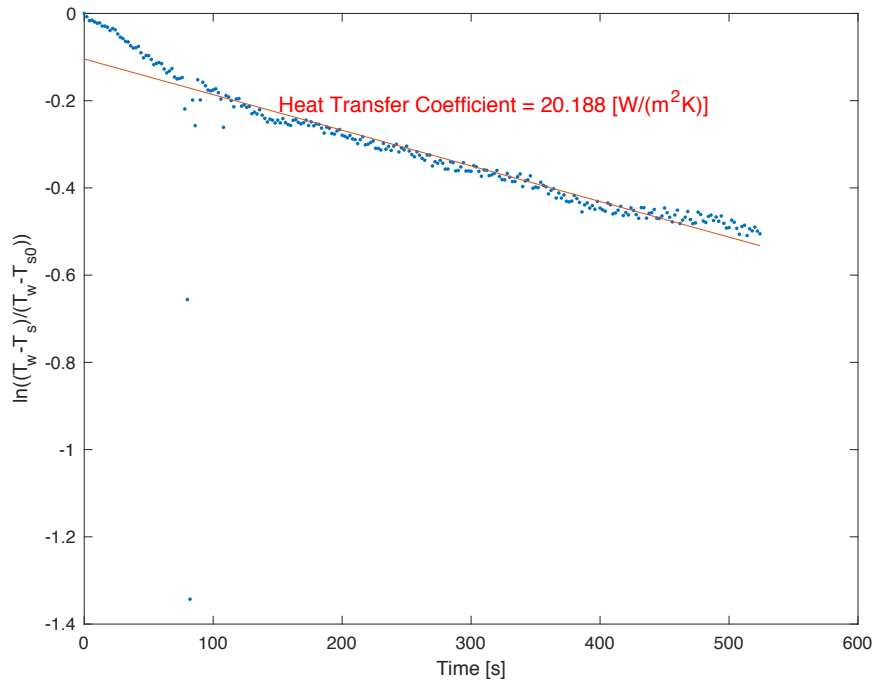


Figure B5. Case 1, 10 % fill level, 6 rpm, Trial 2.

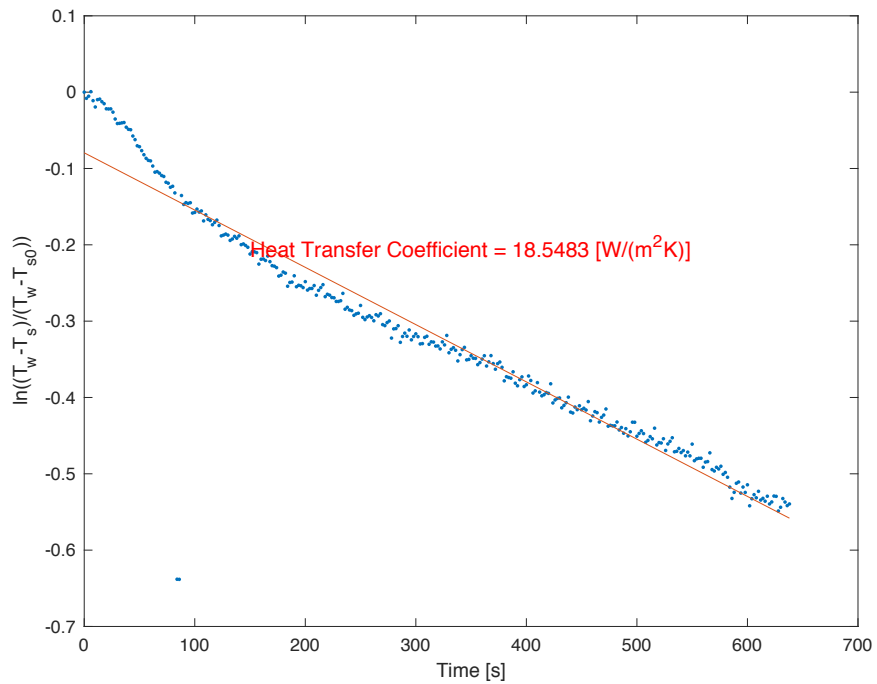


Figure B6. Case 1, 10 % fill level, 6 rpm, Trial 3.

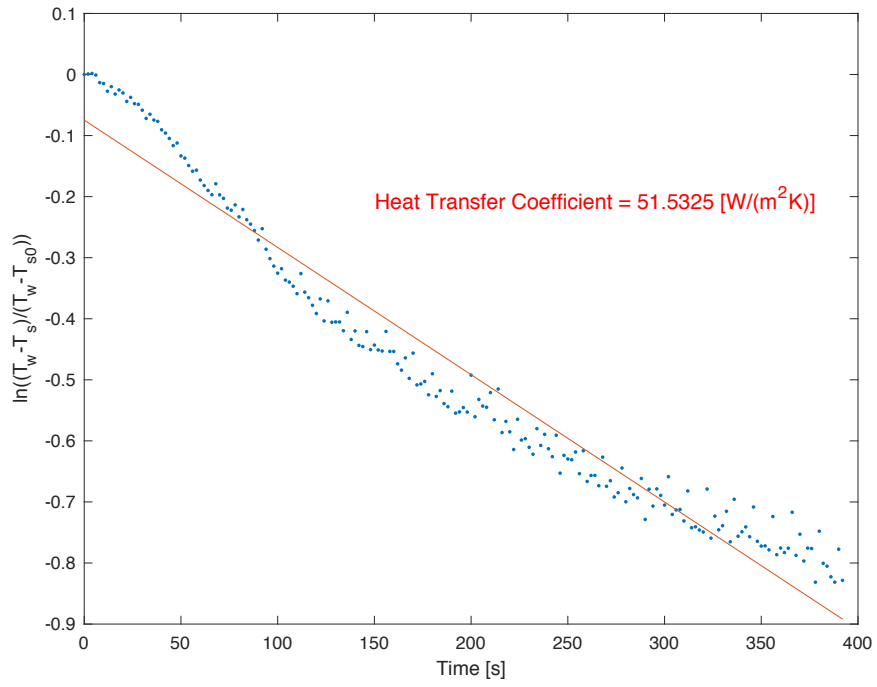


Figure B7. Case 1, 10 % fill level, 10 rpm, Trial 1.

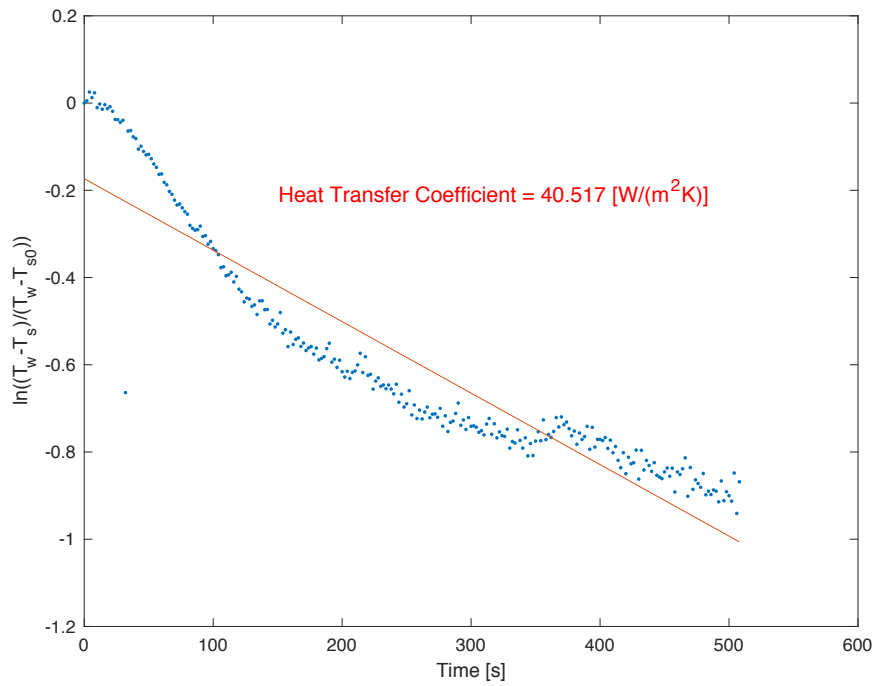


Figure B8. Case 1, 10 % fill level, 10 rpm, Trial 2.

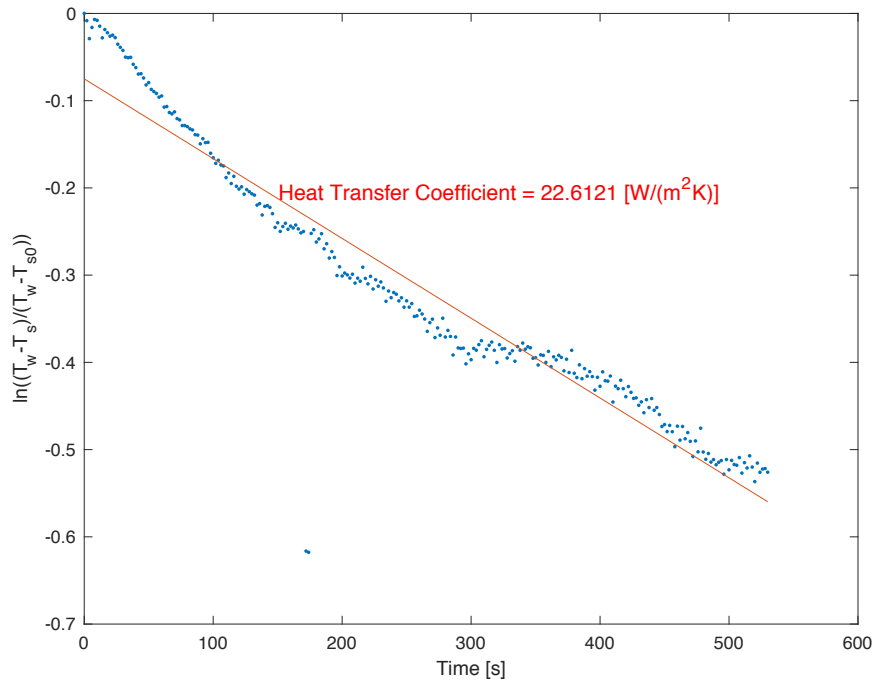


Figure B9. Case 1, 10 % fill level, 10 rpm, Trial 3.

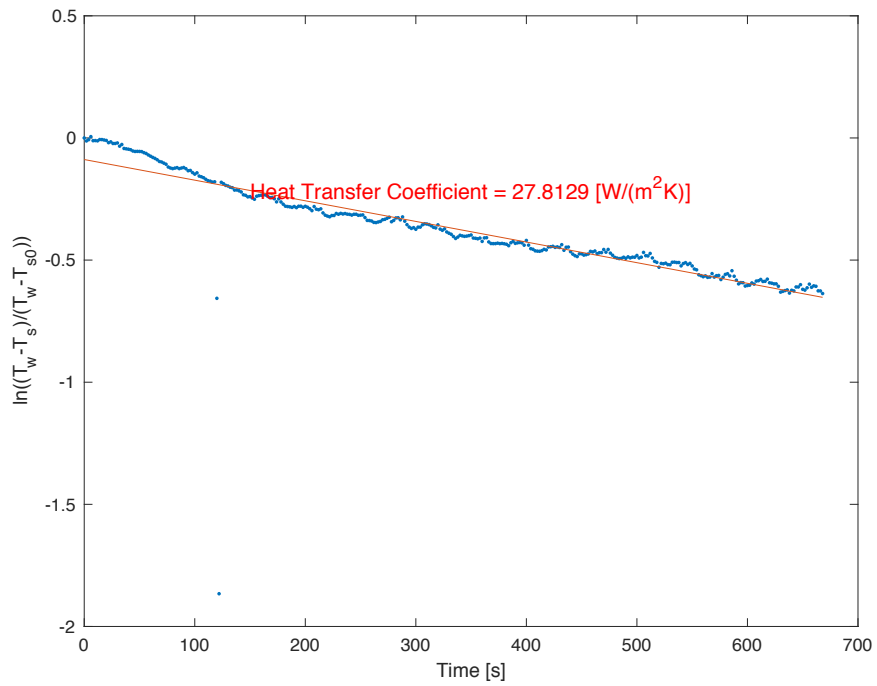


Figure B10. Case 1, 17.5 % fill level, 2 rpm, Trial 1.



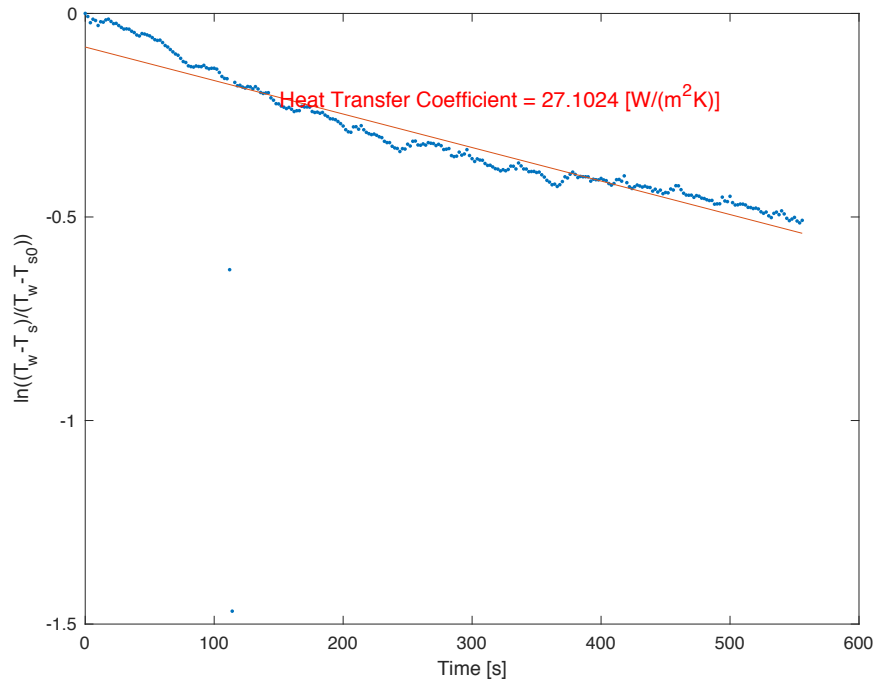


Figure B11. Case 1, 17.5 % fill level, 2 rpm, Trial 2.

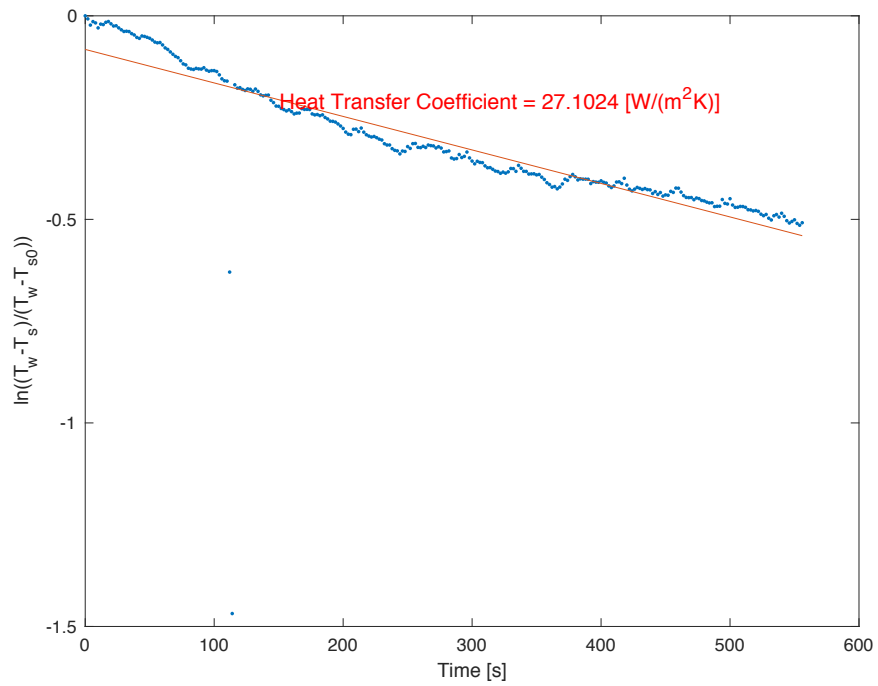


Figure B12. Case 1, 17.5 % fill level, 2 rpm, Trial 3.

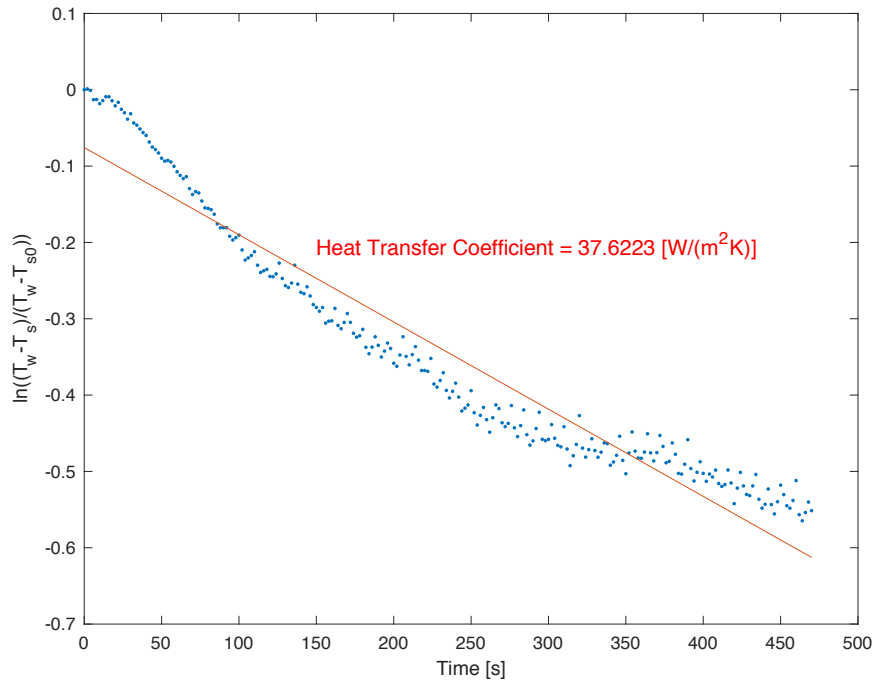


Figure B13. Case 1, 17.5 % fill level, 6 rpm, Trial 1.

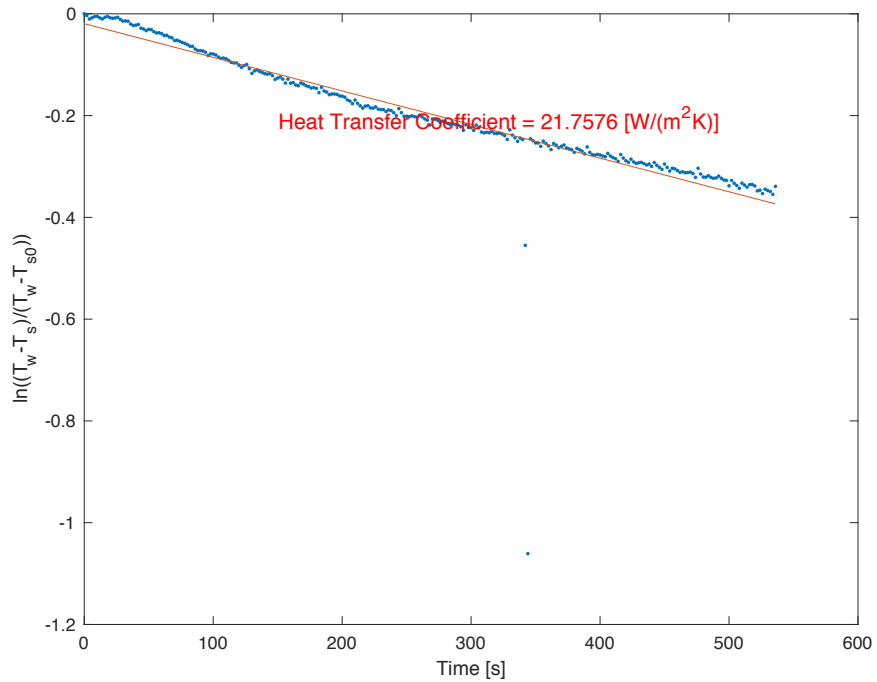


Figure B14. Case 1, 17.5 % fill level, 6 rpm, Trial 2.

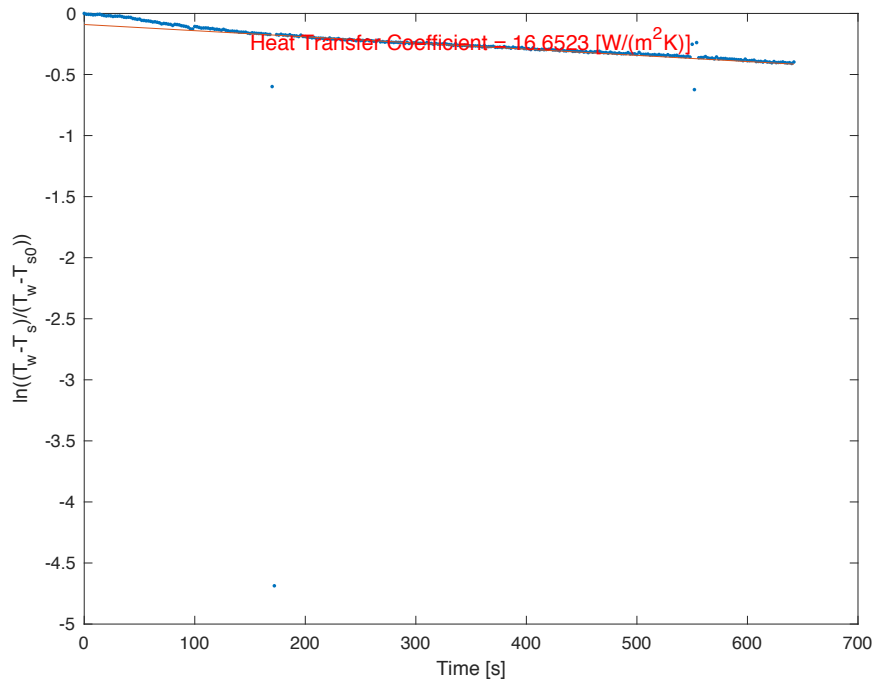


Figure B15. Case 1, 17.5 % fill level, 6 rpm, Trial 3.

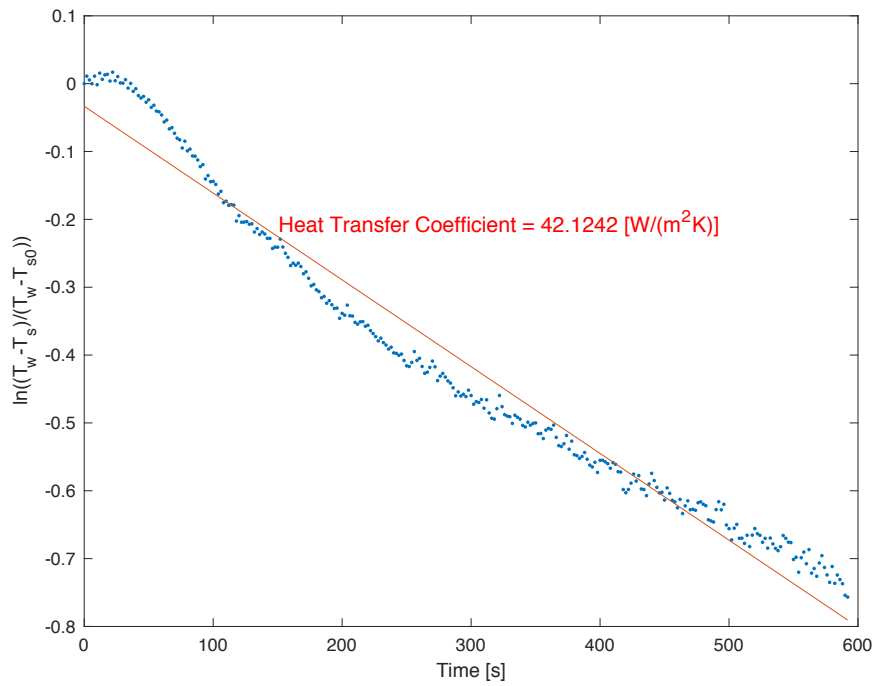


Figure B16. Case 1, 17.5 % fill level, 10 rpm, Trial 1.

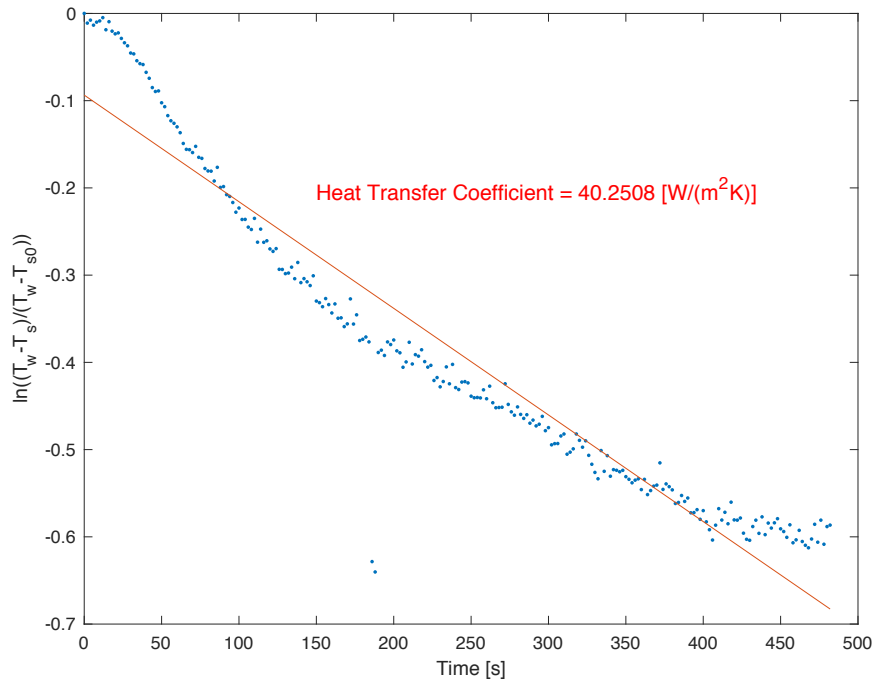


Figure B17. Case 1, 17.5 % fill level, 10 rpm, Trial 2.

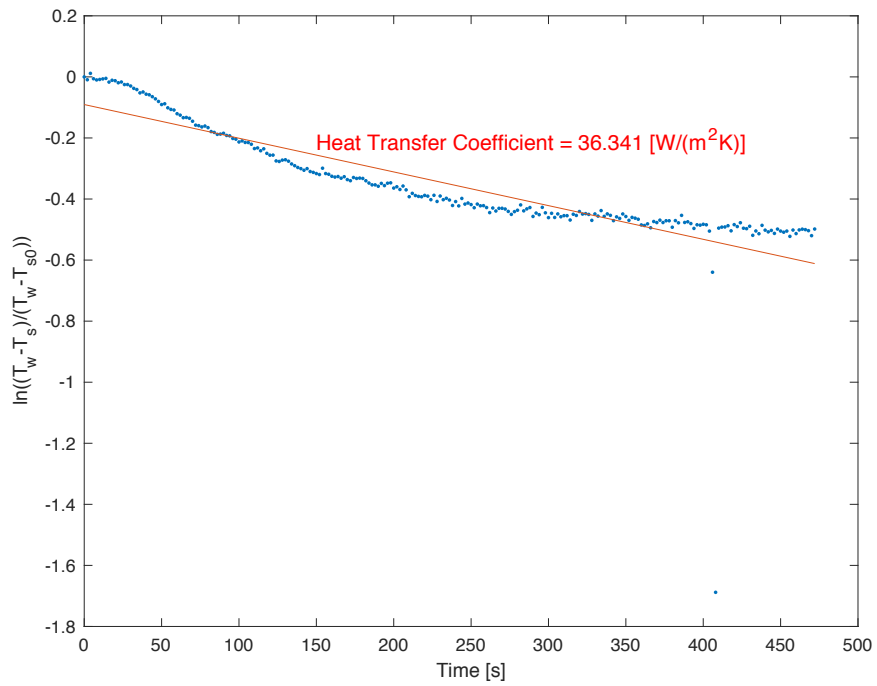


Figure B18. Case 1, 17.5 % fill level, 10 rpm, Trial 3.

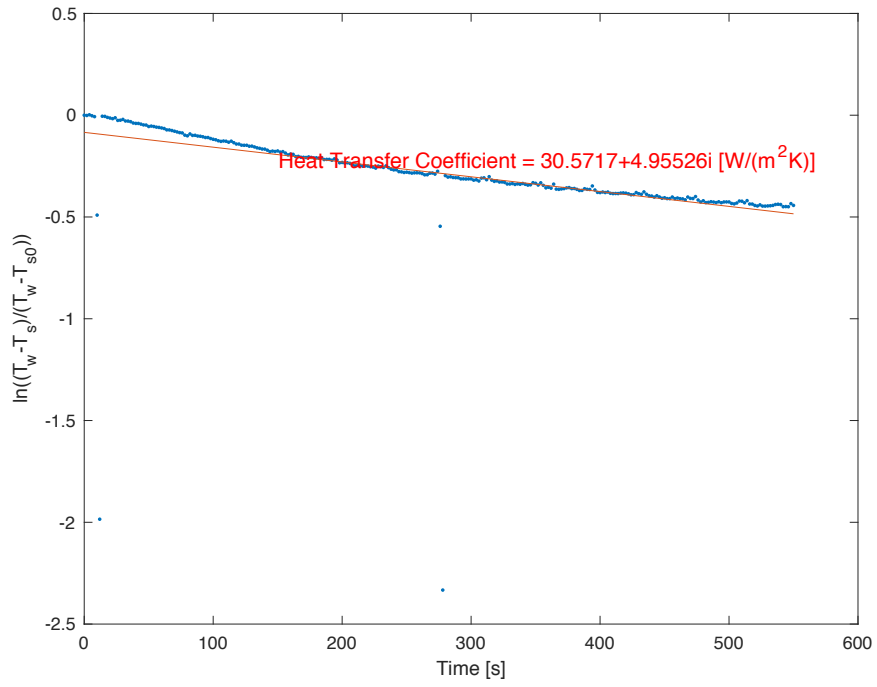


Figure B19. Case 1, 25 % fill level, 2 rpm, Trial 1.

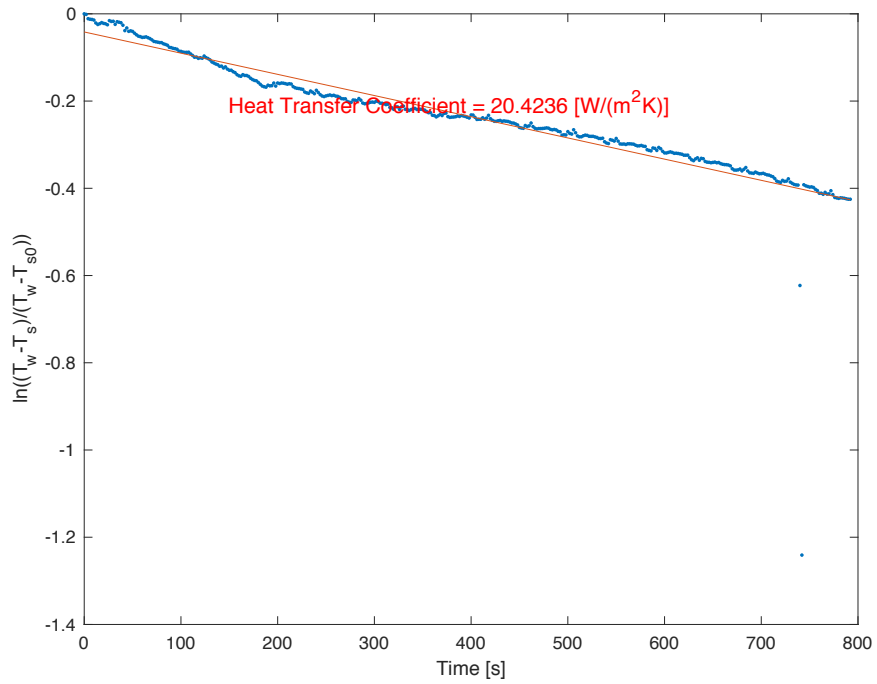


Figure B20. Case 1, 25 % fill level, 2 rpm, Trial 2.

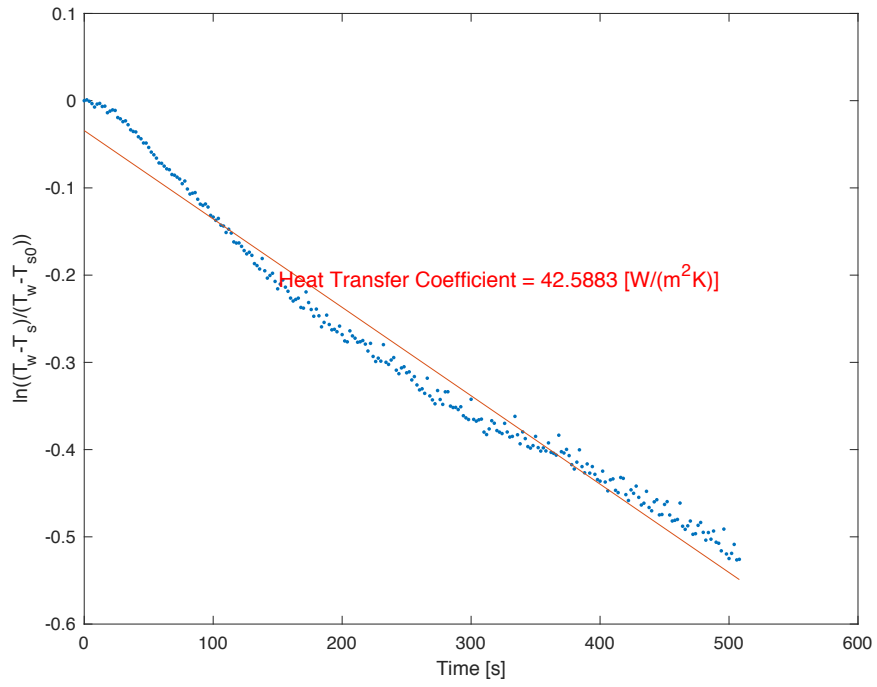


Figure B21. Case 1, 25 % fill level, 6 rpm, Trial 1.

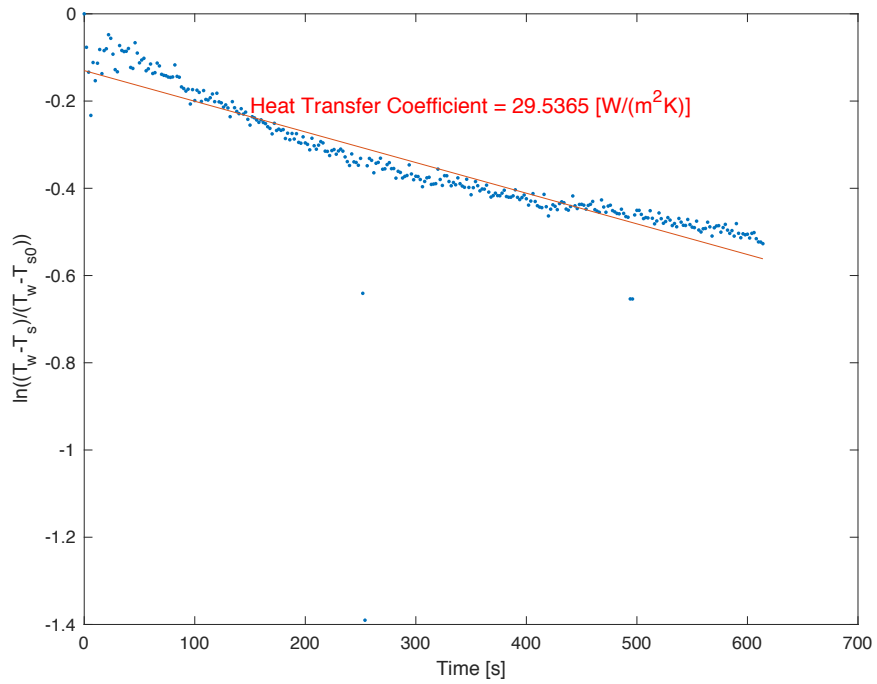


Figure B22. Case 1, 25 % fill level, 6 rpm, Trial 2.

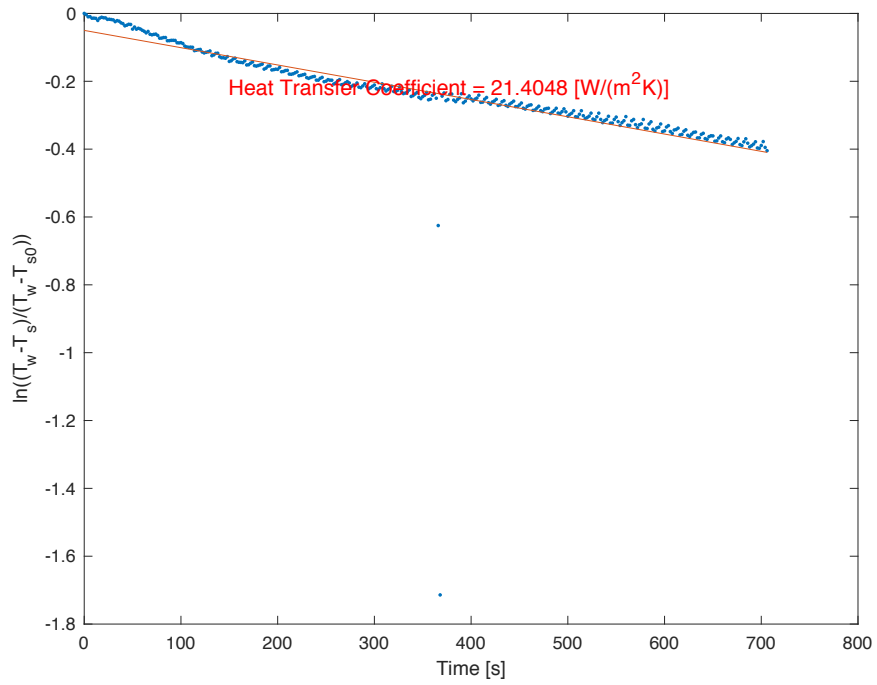


Figure B23. Case 1, 25 % fill level, 6 rpm, Trial 3.

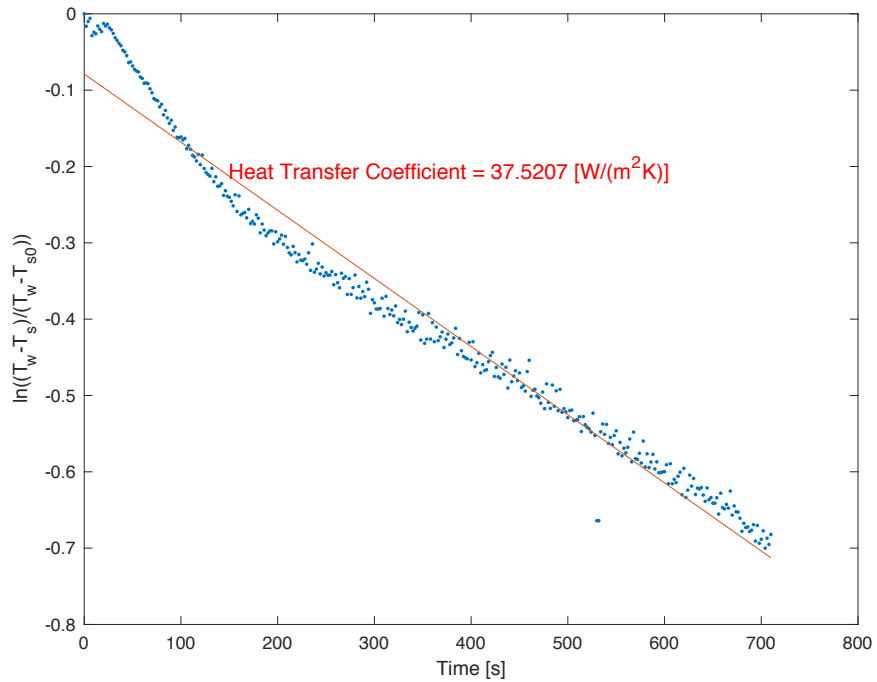


Figure B24. Case 1, 25 % fill level, 10 rpm, Trial 1.

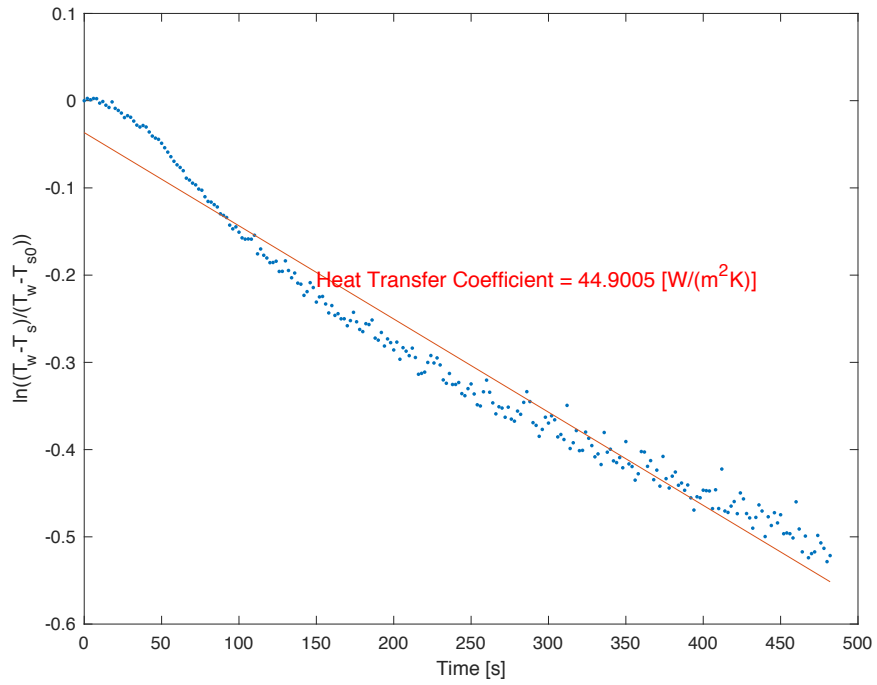


Figure B25. Case 1, 25 % fill level, 10 rpm, Trial 2.

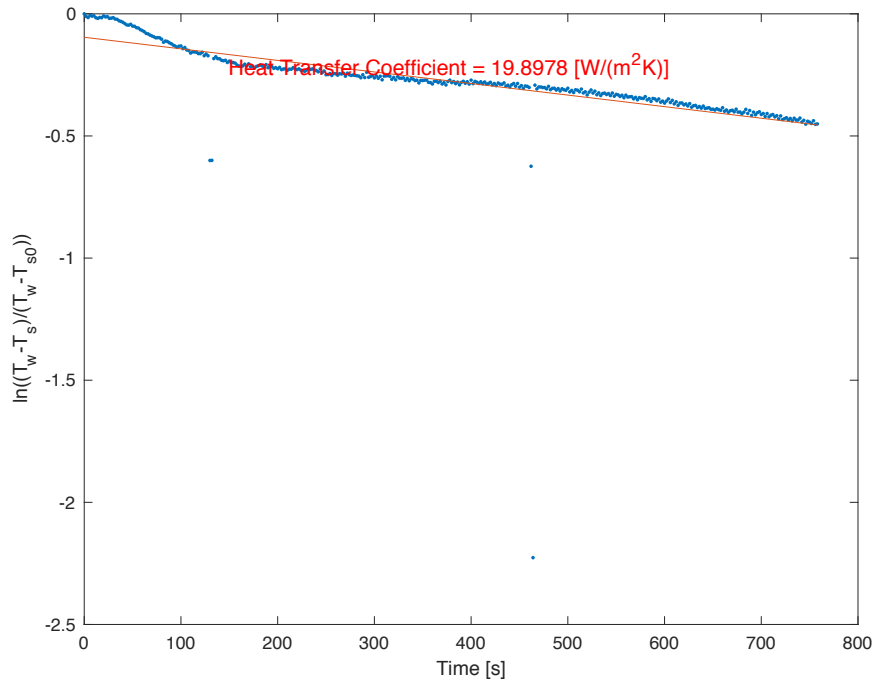


Figure B26. Case 1, 25 % fill level, 10 rpm, Trial 3.



## Case 2 Experiments (Conduction with Convection)

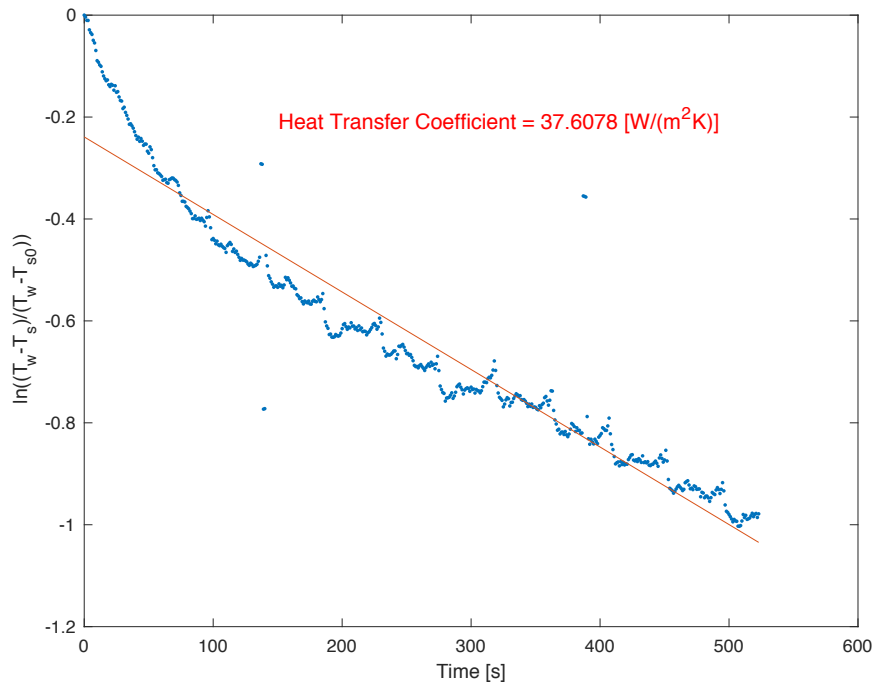


Figure B27. Case 2, 10 % fill level, 2 rpm, Trial 1.

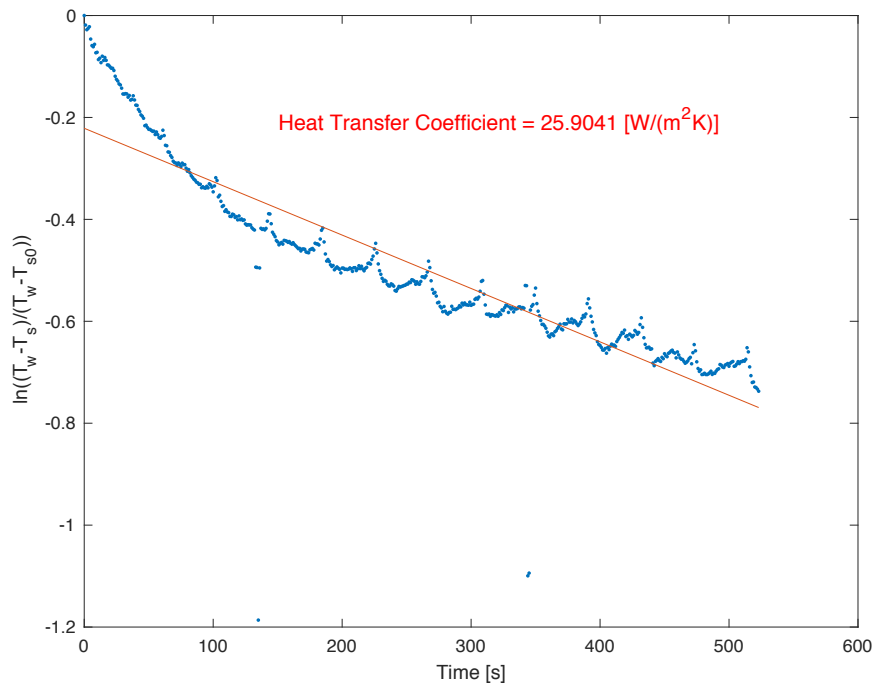


Figure B28. Case 2, 10 % fill level, 2 rpm, Trial 2.

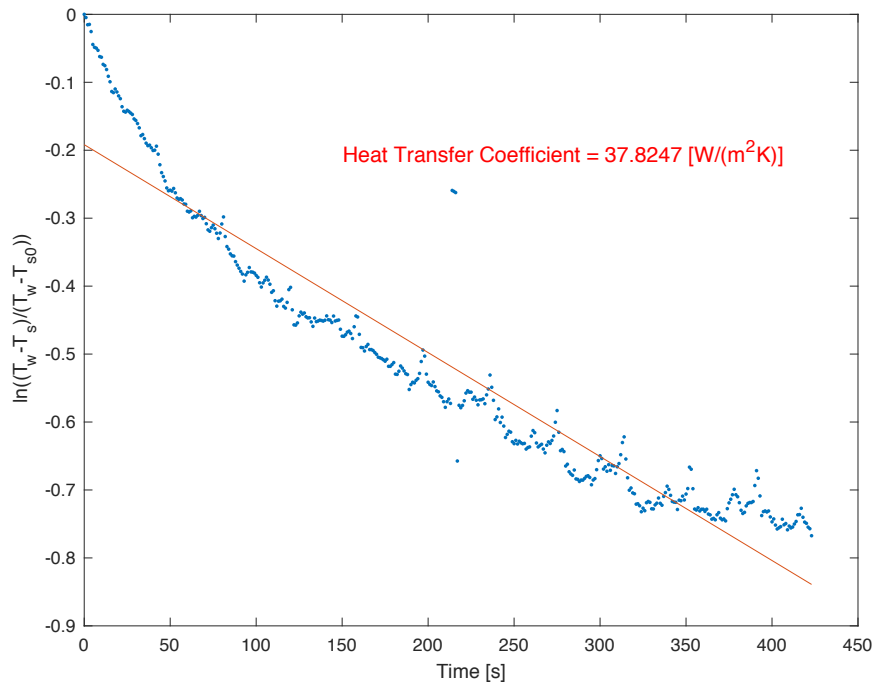


Figure B29. Case 2, 10 % fill level, 2 rpm, Trial 3.

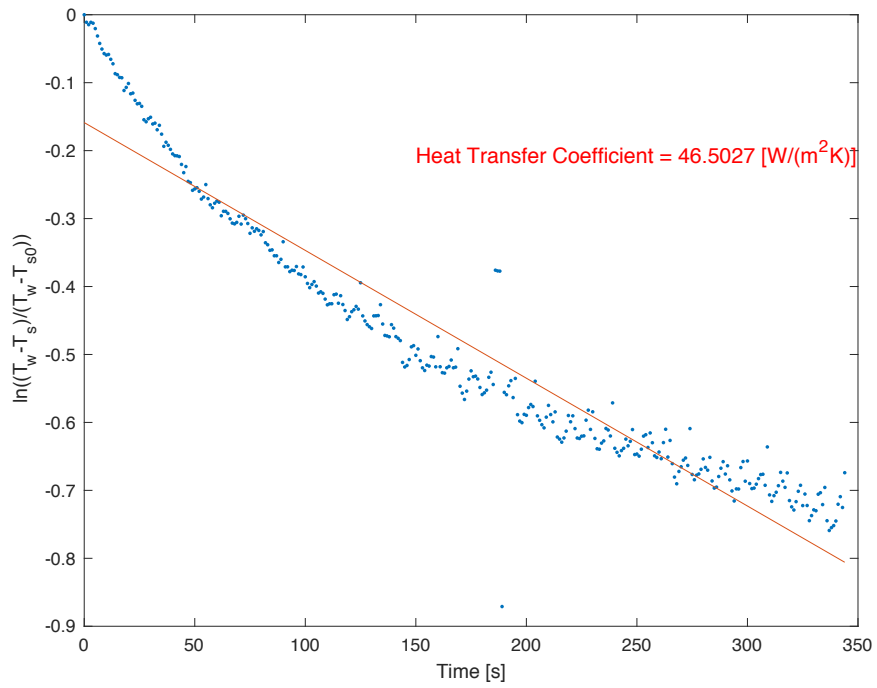


Figure B30. Case 2, 10 % fill level, 6 rpm, Trial 1.

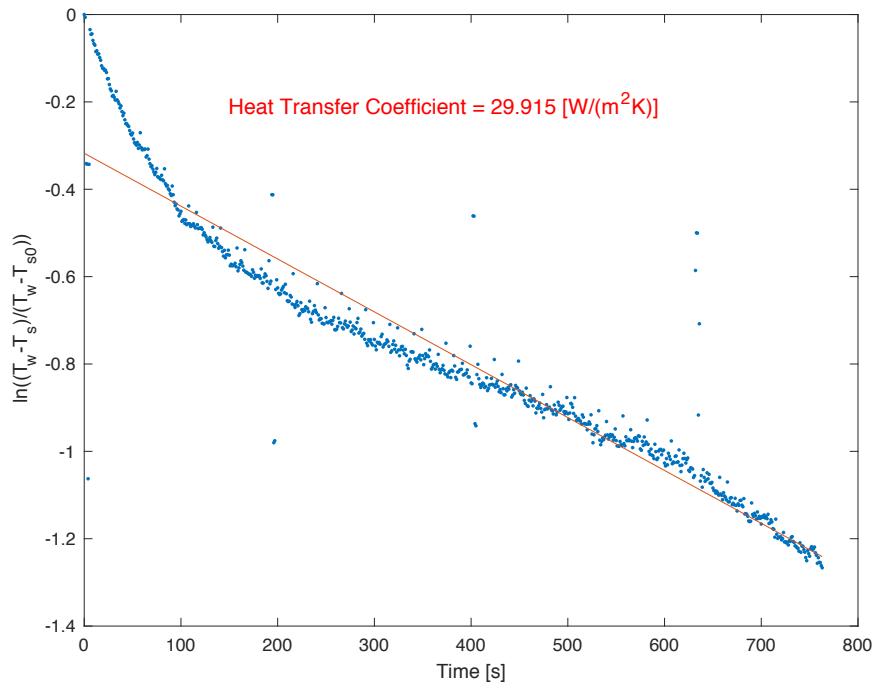


Figure B31. Case 2, 10 % fill level, 6 rpm, Trial 2.

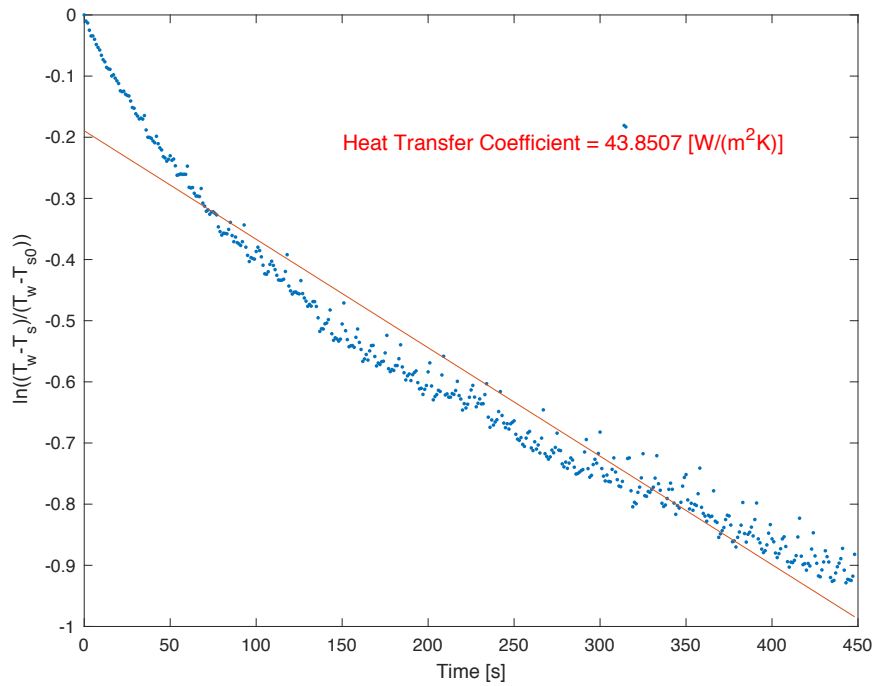


Figure B32. Case 2, 10 % fill level, 6 rpm, Trial 3.

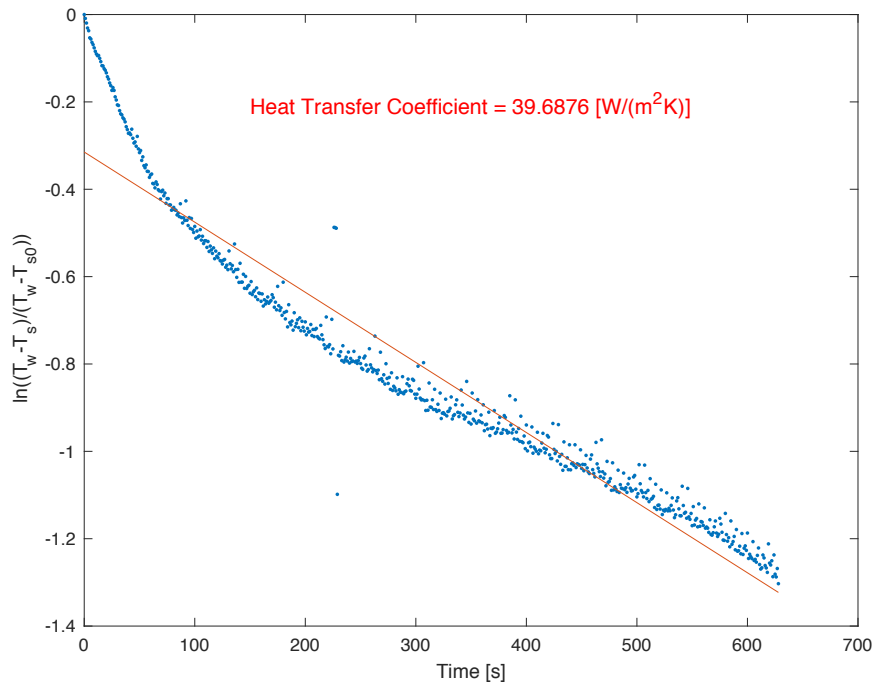


Figure B33. Case 2, 10 % fill level, 10 rpm, Trial 1.

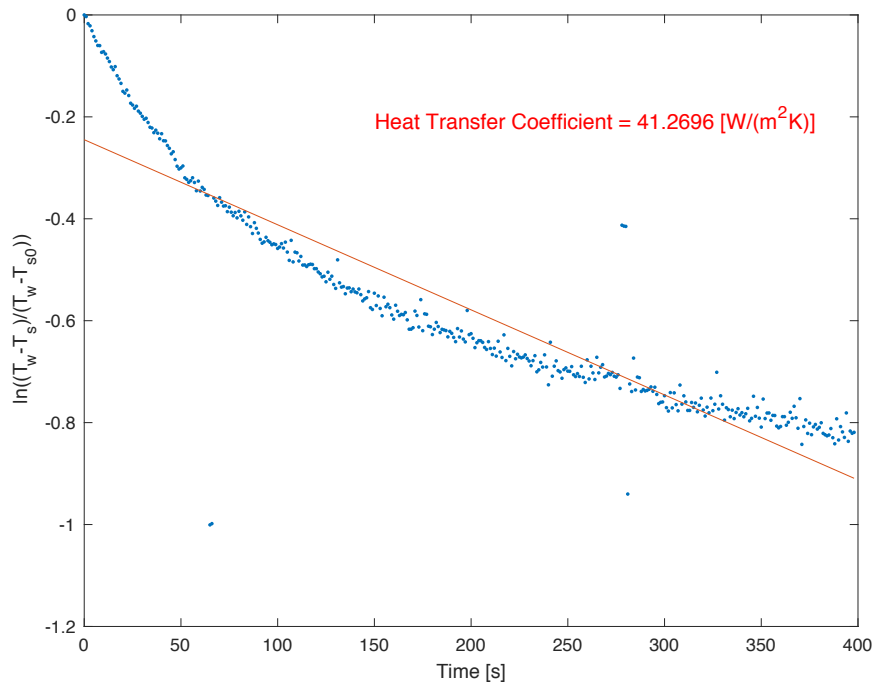


Figure B34. Case 2, 10 % fill level, 10 rpm, Trial 2.

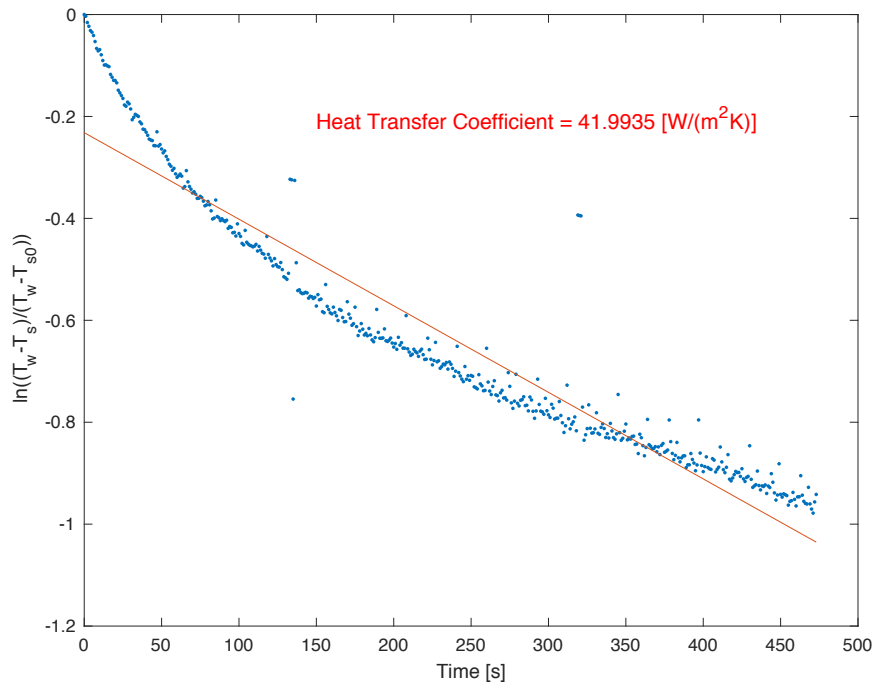


Figure B35. Case 2, 10 % fill level, 10 rpm, Trial 3.

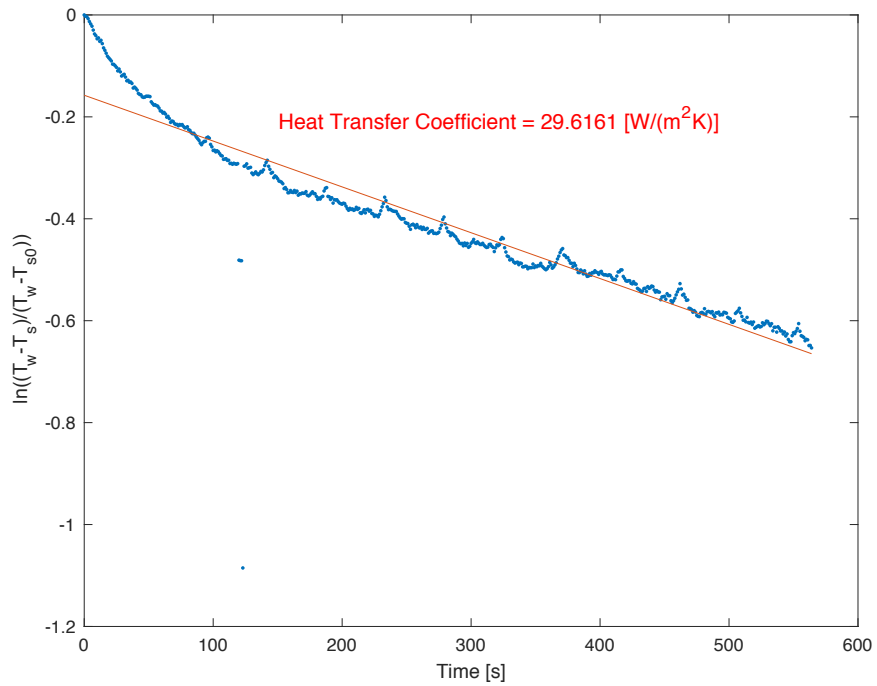


Figure B36. Case 2, 17.5 % fill level, 2 rpm, Trial 1.

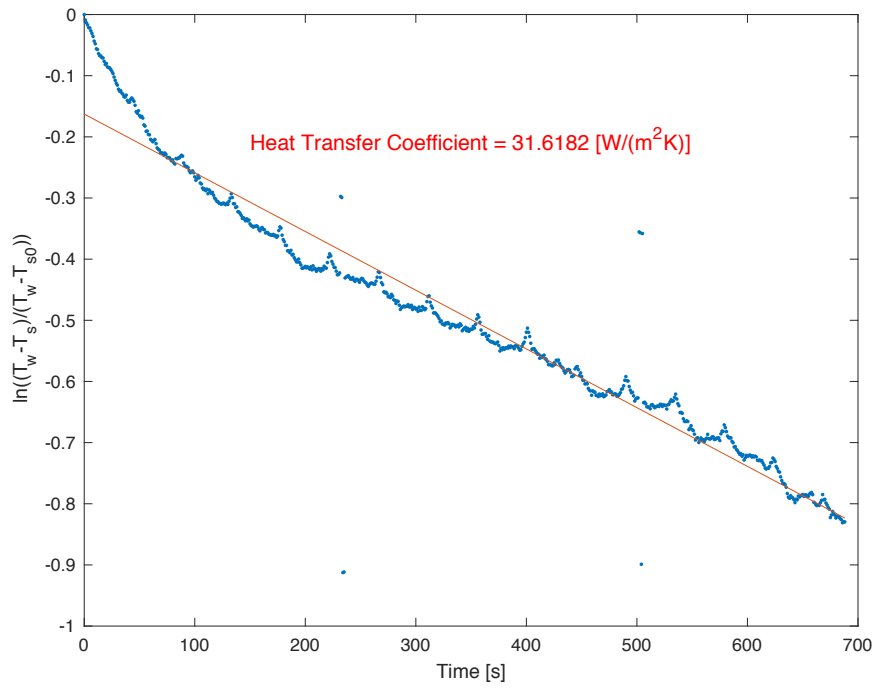


Figure B37. Case 2, 17.5 % fill level, 2 rpm, Trial 2.

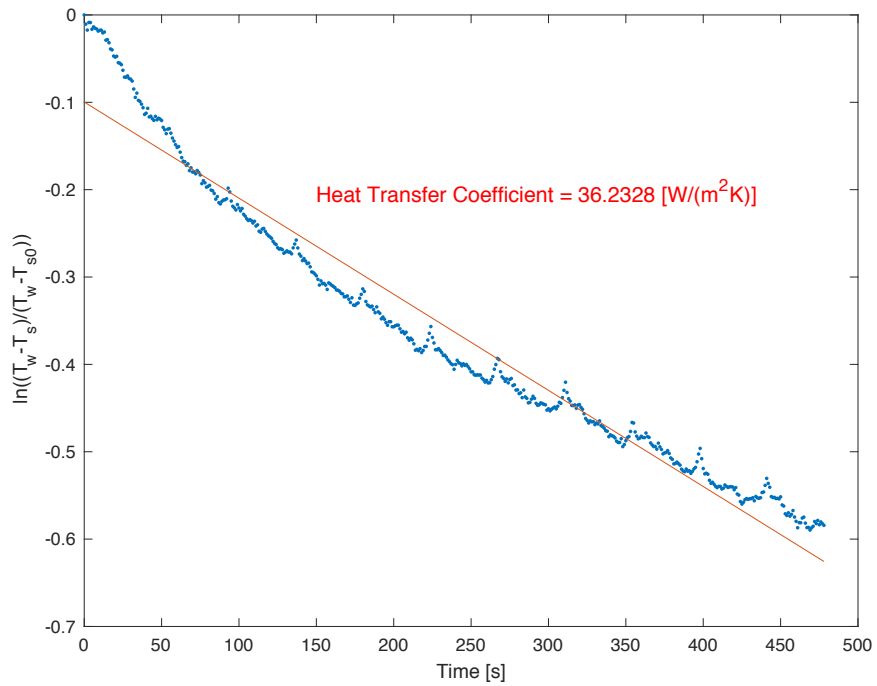


Figure B38. Case 2, 17.5 % fill level, 2 rpm, Trial 3.

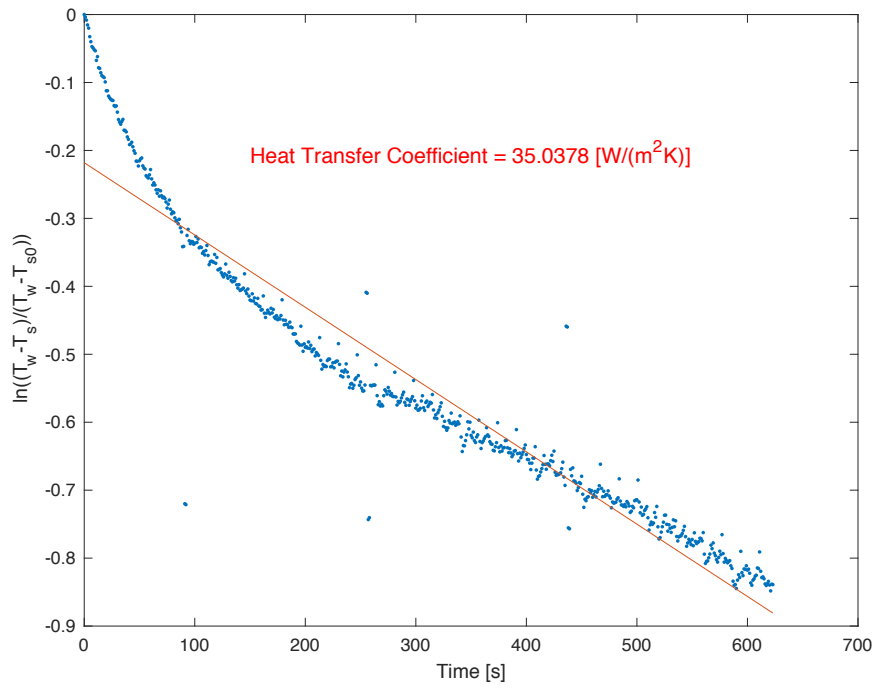


Figure B39. Case 2, 17.5 % fill level, 6 rpm, Trial 1.

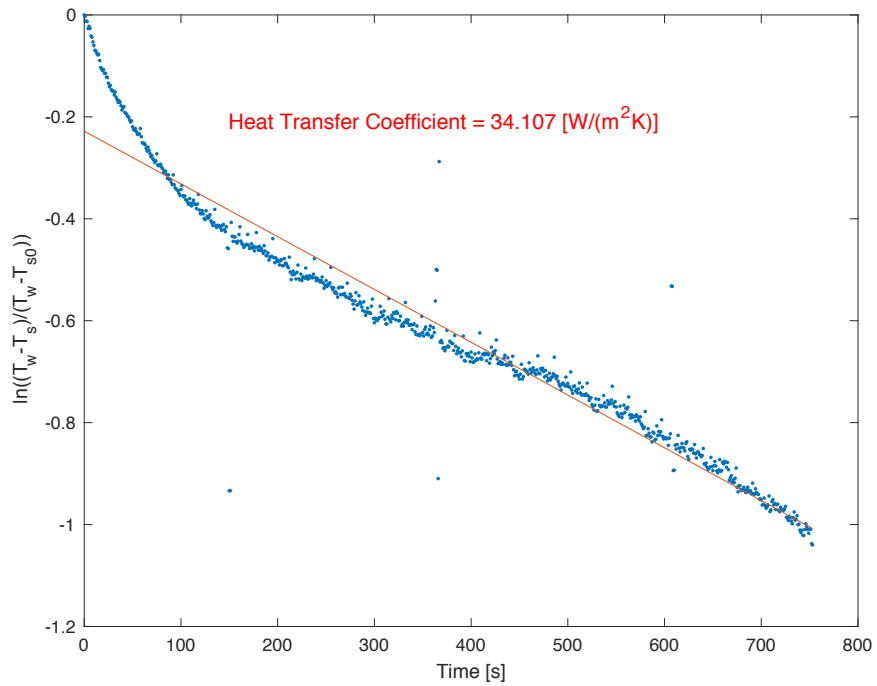


Figure B40. Case 2, 17.5 % fill level, 6 rpm, Trial 2.

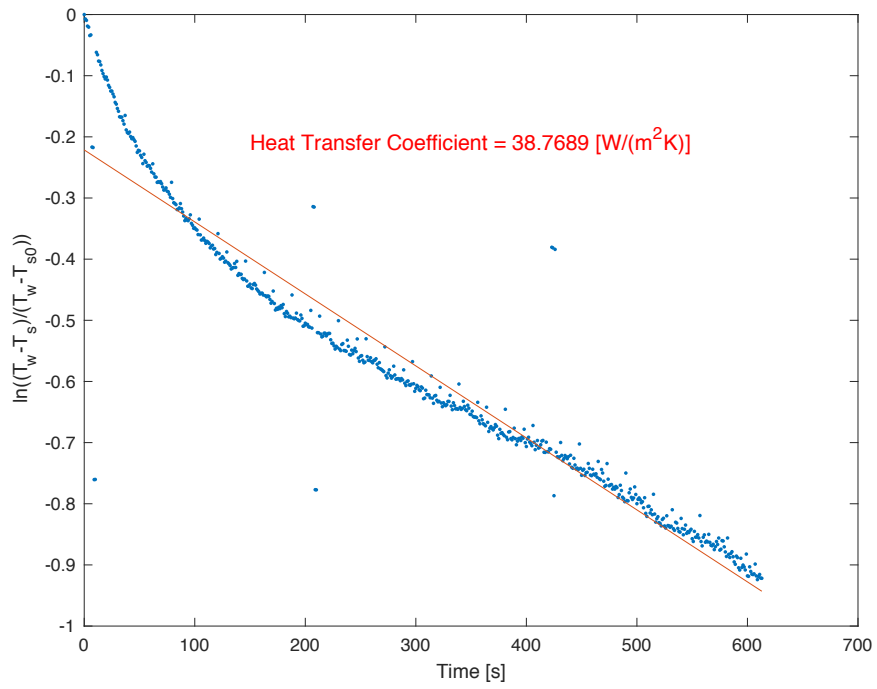


Figure B41. Case 2, 17.5 % fill level, 6 rpm, Trial 3.

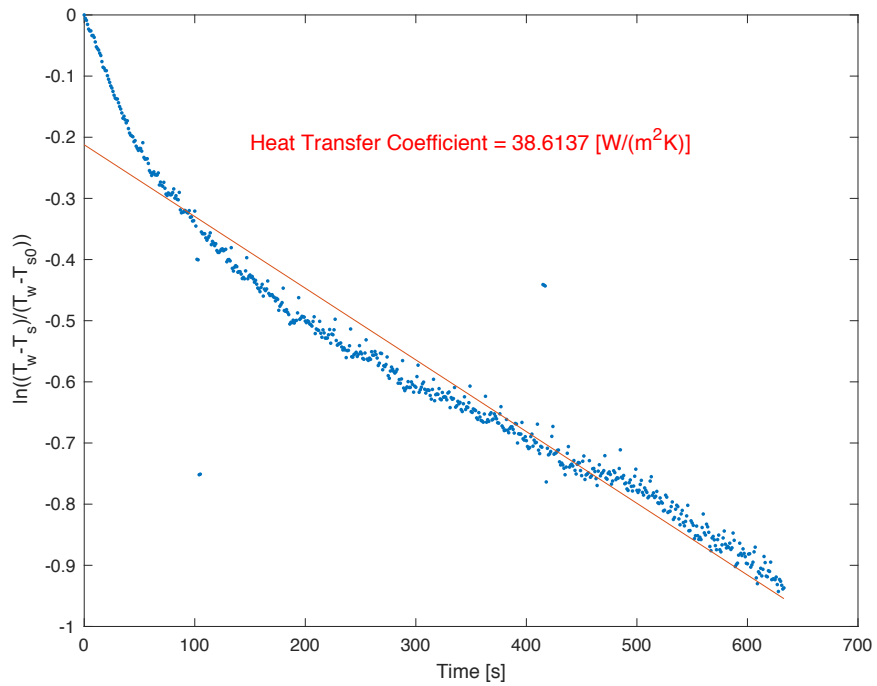


Figure B42. Case 2, 17.5 % fill level, 10 rpm, Trial 1.



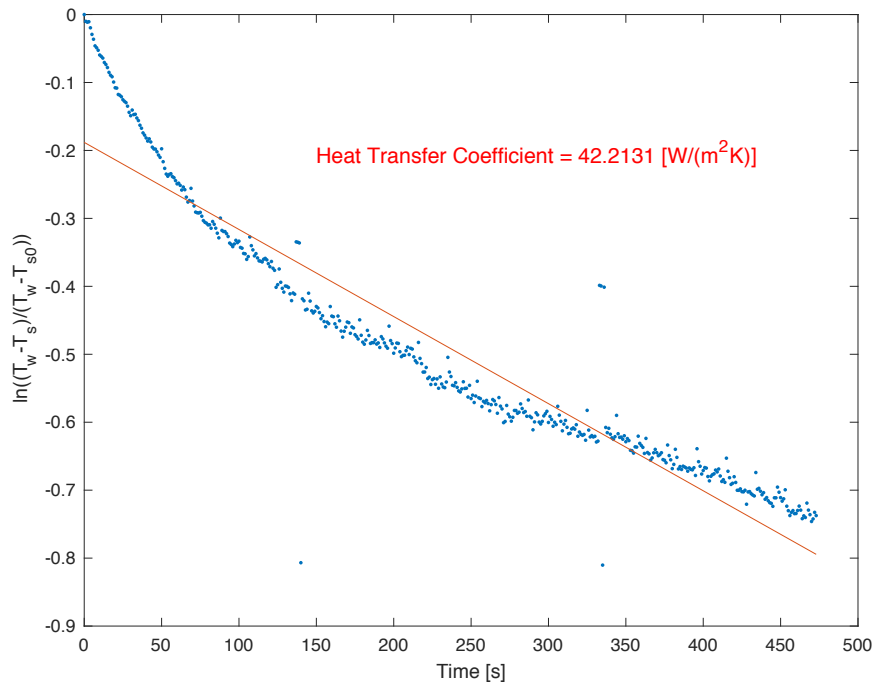


Figure B43. Case 2, 17.5 % fill level, 10 rpm, Trial 2.

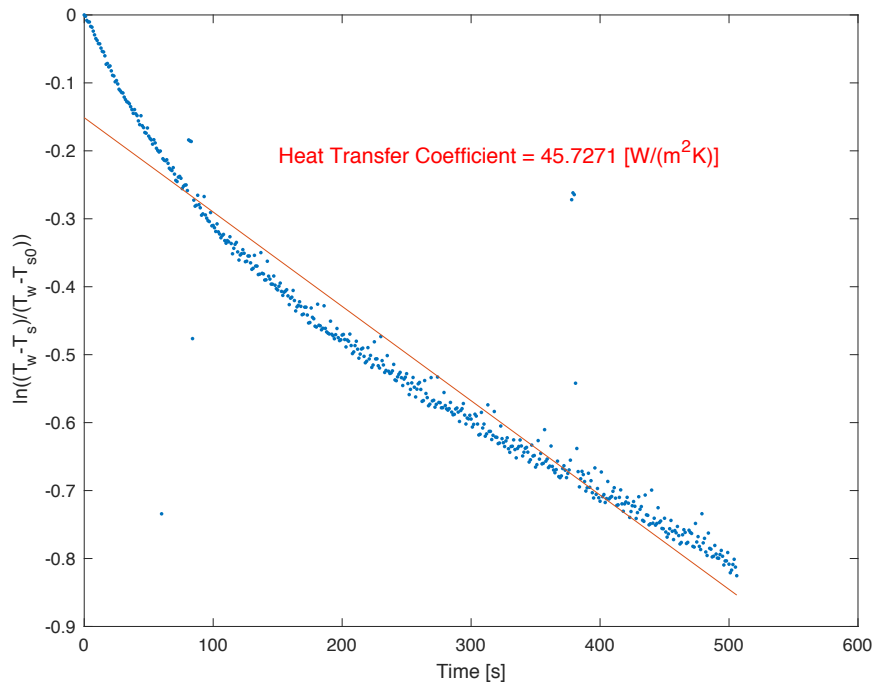


Figure B44. Case 2, 17.5 % fill level, 10 rpm, Trial 3.

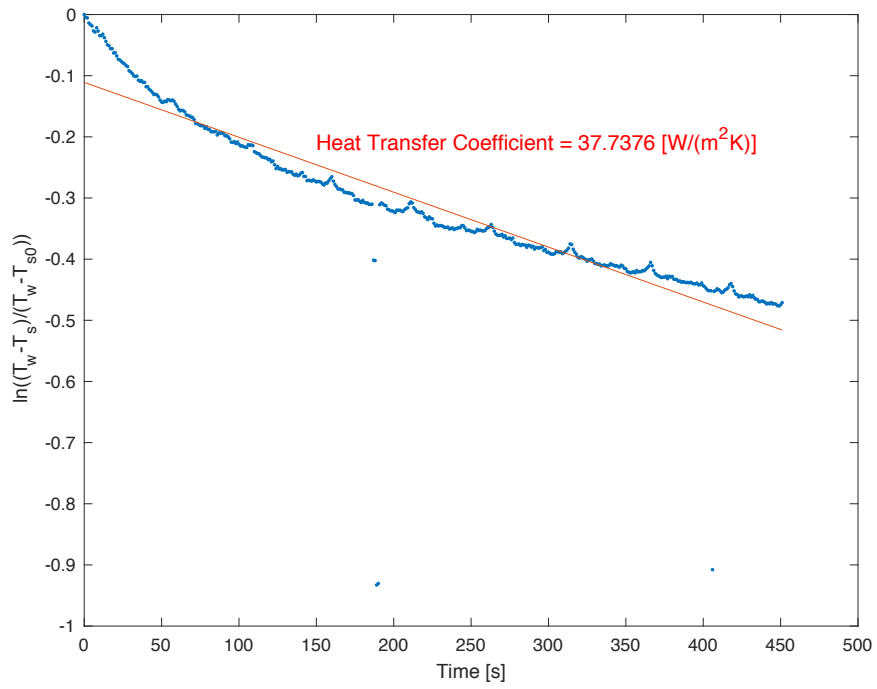


Figure B45. Case 2, 25 % fill level, 2 rpm, Trial 1.

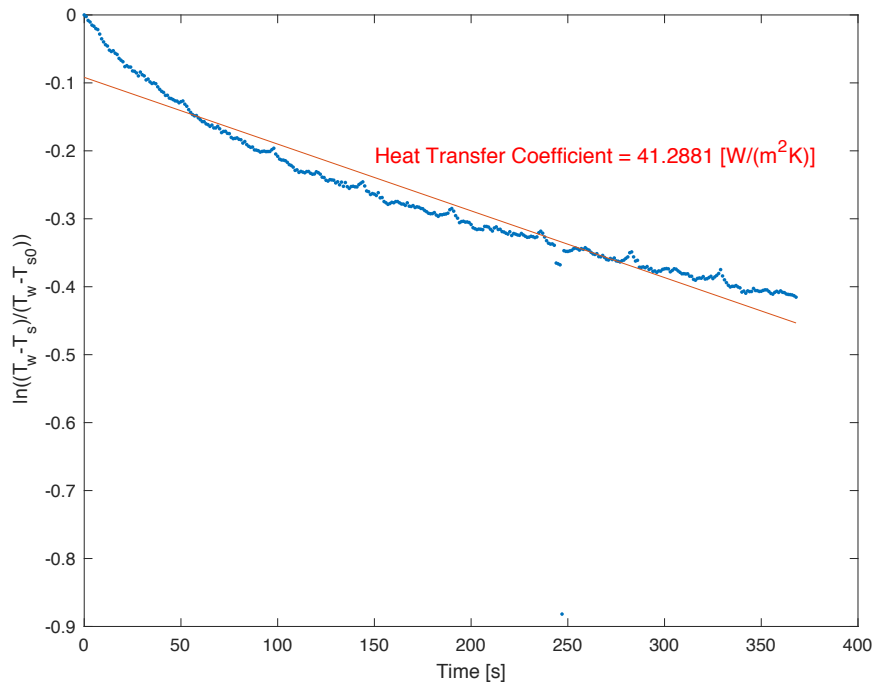


Figure B46. Case 2, 25 % fill level, 2 rpm, Trial 2.

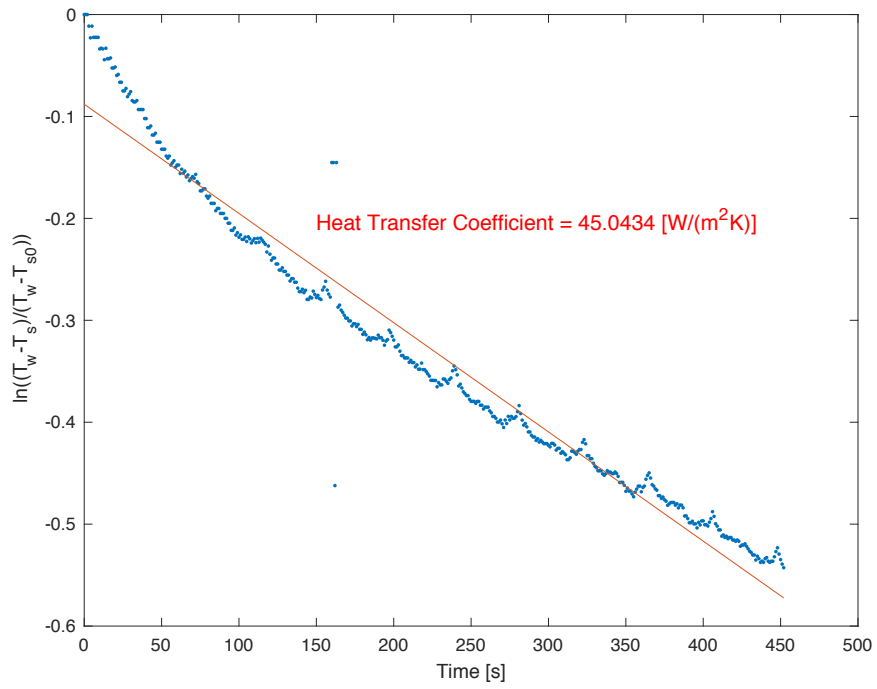


Figure B47. Case 2, 25 % fill level, 2 rpm, Trial 3.

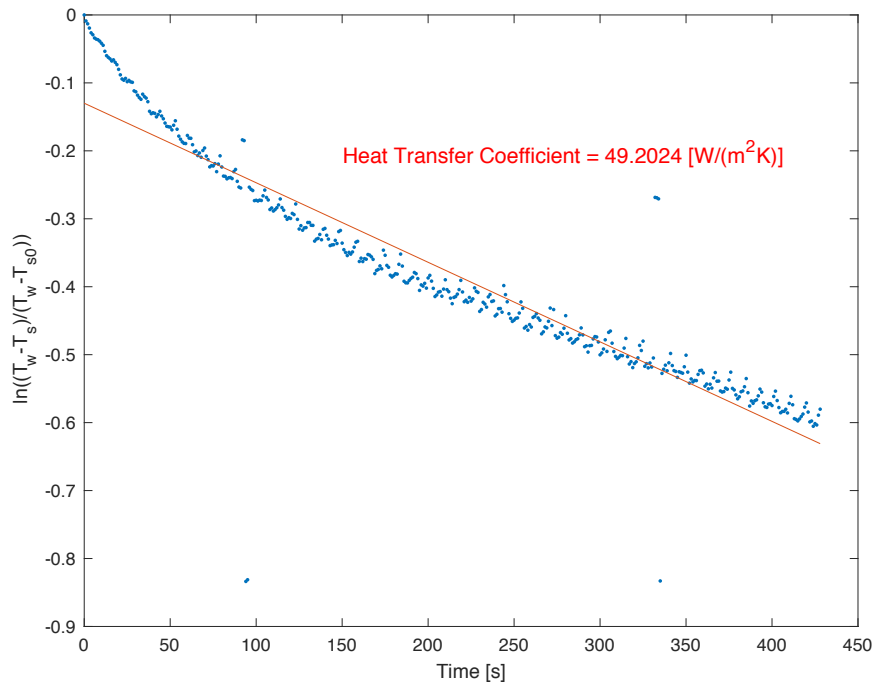


Figure B48. Case 2, 25 % fill level, 6 rpm, Trial 1.

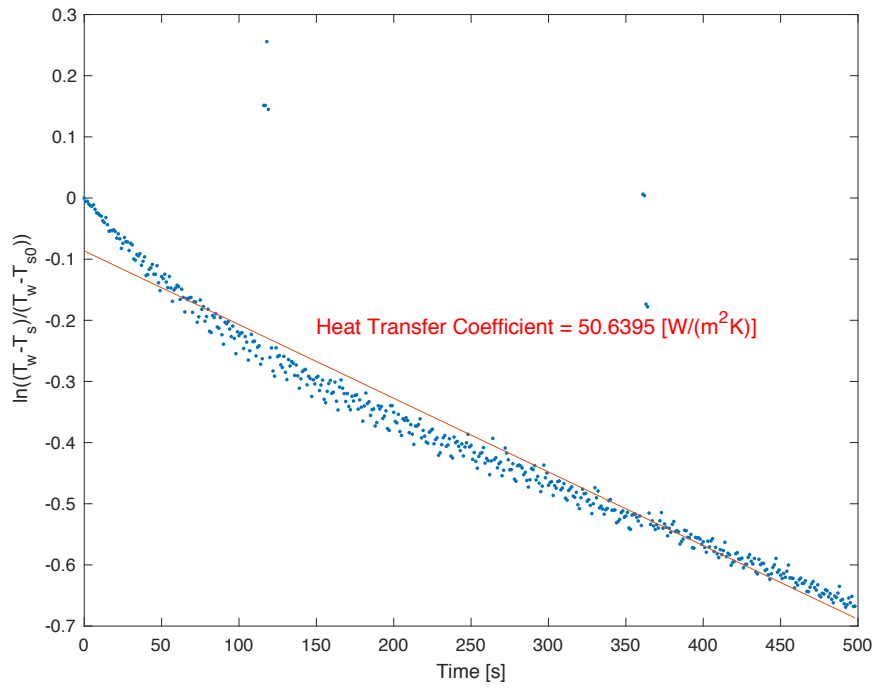


Figure B49. Case 2, 25 % fill level, 6 rpm, Trial 2.

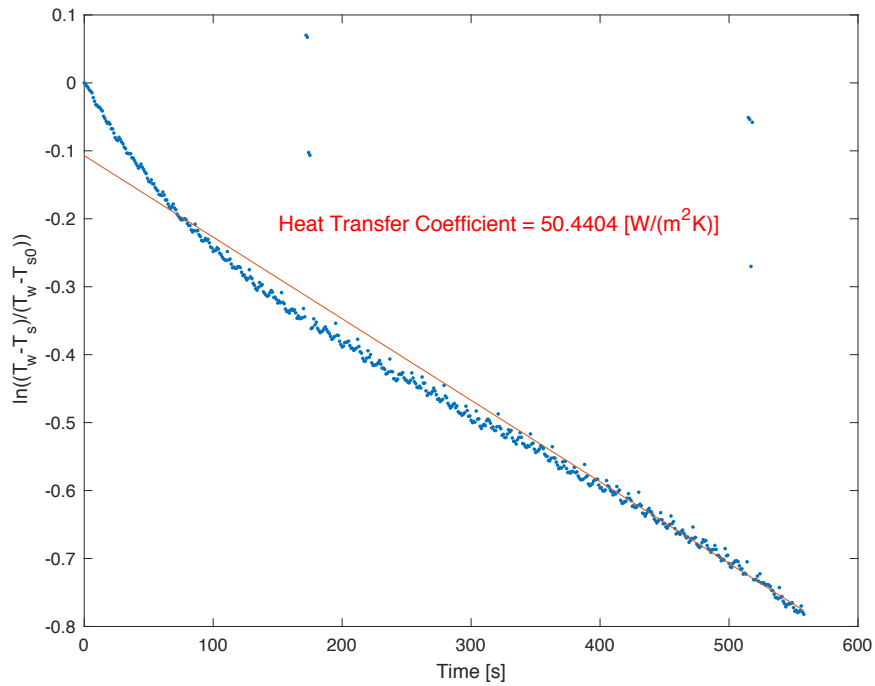


Figure B50. Case 2, 25 % fill level, 6 rpm, Trial 3.

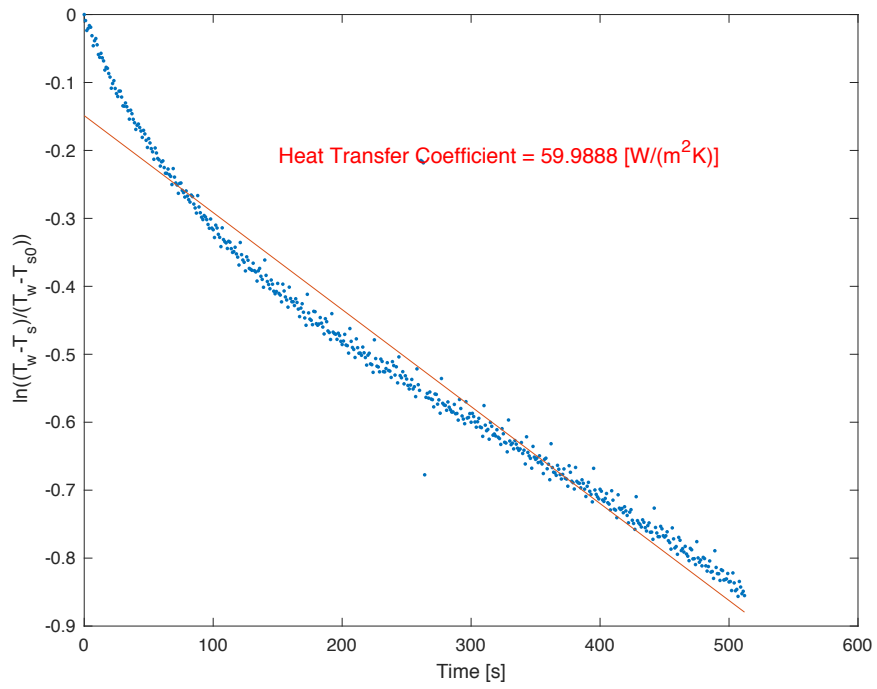


Figure B51. Case 2, 25 % fill level, 10 rpm, Trial 1.

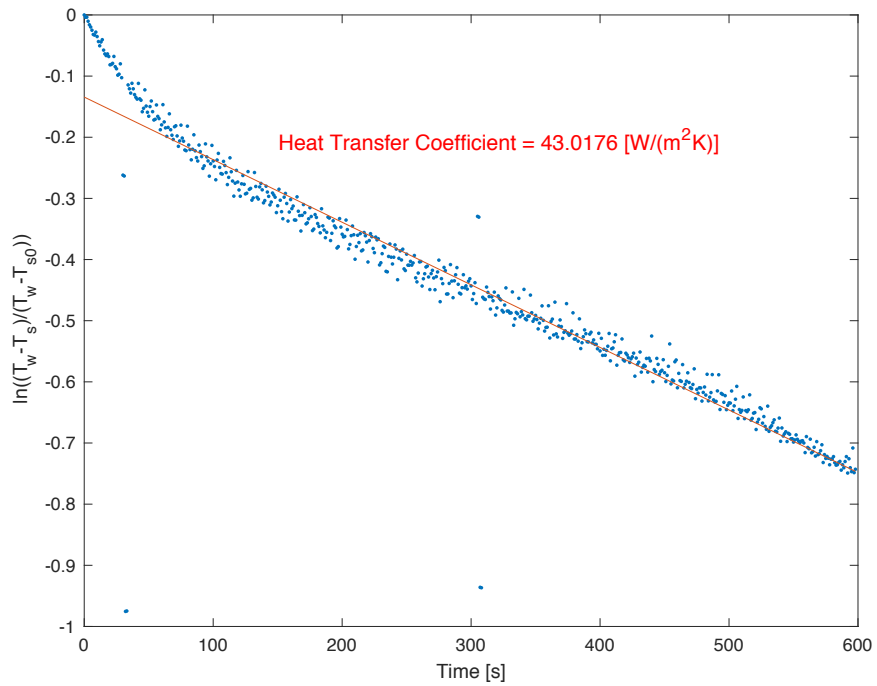


Figure B52. Case 2, 25 % fill level, 10 rpm, Trial 2.

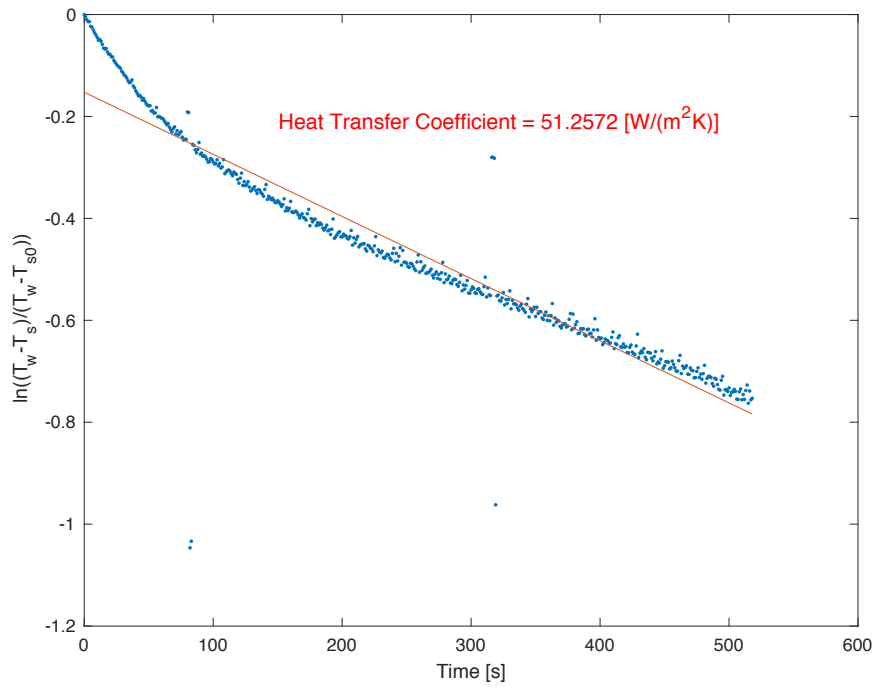


Figure B53. Case 2, 25 % fill level, 10 rpm, Trial 3.